

Noncrossing Approximation for the Anisotropic Kondo Model: Charge Fluctuations in a Quantum Box

Eran Lebanon, Avraham Schiller, and Vilen Zevin

Racah Institute of Physics, The Hebrew University, Jerusalem 91904, Israel

(November 1, 2018)

The noncrossing approximation (NCA) is generalized to the multi-channel Kondo-spin Hamiltonian with arbitrary anisotropic exchange couplings and an external magnetic field, and applied — in the framework of Matveev’s mapping — to the charge fluctuations in a single-electron box at the Coulomb blockade. The temperature dependences of the charge step and the capacitance are calculated for a narrow point contact. At low temperatures and close to the degeneracy point, the capacitance line shape exhibits an approximate scaling with U/\sqrt{T} , where U is the deviation in gate voltage from the degeneracy point. This scaling relation is proposed as a sharp experimental diagnostic for the non-Fermi-liquid physics of the system at low temperatures. Both the reliability and shortcomings of the Kondo NCA are discussed in detail. Through comparison with poor-man’s scaling, we are able to pinpoint the omission of particle-particle processes as the origin of the NCA flaws. An extended diagrammatic scheme is devised to amend the NCA flaws.

PACS numbers: 72.15.Qm, 73.23.Hk, 75.20.Hr

I. INTRODUCTION

The rapid development of nanofabrication techniques has opened new possibilities for the study of the Kondo effect in mesoscopic systems. Using ultra small quantum dots it is now possible to measure Kondo-assisted tunneling through a single tunable magnetic impurity.^{1–5} Using scanning tunneling spectroscopy, one can directly probe the local electronic structure around an isolated magnetic adatom on a metallic surface.^{6–8} It is even becoming experimentally feasible to address the competition between intersite magnetic locking and Kondo-type correlations in the two-impurity cluster.^{9,10} Perhaps most intriguing, though, are the possible realizations of the two-channel Kondo effect,^{11,12} which is a prototype for a non-Fermi-liquid ground state in correlated electron systems.¹³

There are several leading candidates for the observation of the two-channel Kondo effect in mesoscopic systems. Most notably, zero-bias anomalies seen in metallic point contacts,^{14–16} which feature square-root temperature and voltage dependence of the differential conductance; scaling of the differential conductance with $eV/k_B T$ (eV being the applied bias); and the absence of a Zeeman splitting under an applied magnetic field — all of which are in line with the notion of two-channel Kondo scattering off nonmagnetic two-level tunneling systems (TLS).^{13,17} Two-channel Kondo scattering off TLS was also recently invoked¹⁸ to explain the shape and scaling behavior of the out-of-equilibrium energy distribution function of quasiparticles in copper and gold wires.¹⁹ In a separate recent experiment on the charging of a semiconductor quantum dot, Berman *et al.*²⁰ observed capacitance line shapes in accordance with Matveev’s prediction for the two-channel Kondo screening of quantum charge fluctuations on the dot.^{21,22} The two nearly degenerate levels in this picture correspond to the two available charge configurations at the Coulomb blockade.

Common to both the TLS and Coulomb-blockade scenarios for the two-channel Kondo effect is a strong anisotropy in the effective spin-exchange interaction. Specifically, in TLS one generically has¹³ $J_z \gg J_x > J_y = 0$ (J_i being the i th component of the effective spin-exchange interaction), while $J_z = 0$ and $J_x = J_y \neq 0$ in the case of the Coulomb blockade.²¹ That the intermediate-coupling fixed point of the two-channel Kondo model is stable against exchange anisotropy is well known from numerical renormalization-group^{23,24} and conformal field theory^{24–26} studies. However, there is a clear lack in quantitative treatments that cover all temperature and field regimes of the model, as is required for each of the two systems mentioned above. This is especially true of the nonequilibrium scattering off TLS, where theoretical efforts have focused on the related $SU(2) \times SU(2)$ two-channel Anderson model,¹⁷ rather than the actual anisotropic Kondo-spin Hamiltonian appropriate for this case. We also note a growing interest in quantitative theories of the single-channel anisotropic Kondo model,²⁷ particularly in connection with the Ohmic dissipative two-state system,^{28–31} and the heavy fermion compound $Ce_{0.8}La_{0.2}Al_3$.^{32,33}

In this paper, we extend the noncrossing approximation³⁴ (NCA) to the Kondo-spin Hamiltonian with arbitrary anisotropic spin-exchange couplings, and apply it to the charge fluctuations in a single-electron box at the Coulomb blockade. The NCA was extensively used in the 80’s to study dilute magnetic alloys, especially Ce- and Yb-based alloys with large orbital degeneracy. Its usefulness for treating the multi-channel Anderson model was later emphasized by Cox and Ruckenstein,³⁵ who noticed that the NCA pathology hampering the single-channel case³⁴ actually corresponds to the exact non-Fermi-liquid power laws and logarithms of the multi-channel Kondo effect. Compared to exact methods such as the Bethe ansatz and conformal field theory, the NCA has the cru-

cial advantage that it is not restricted to idealized models; it could be used to compute dynamical properties over extended temperature and parameter regimes; and it has a natural extension to nonequilibrium.^{17,36} Aside from the Anderson model, the NCA was also applied to the Coqblin-Schrieffer Hamiltonian³⁷ in the form of a self-consistent ladder approximation,³⁸ yet no direct formulation of this approach has been devised to date for the Kondo Hamiltonian.

Generalizing the NCA to the multi-channel Kondo-spin Hamiltonian with arbitrary spin-exchange and potential-scattering couplings, a comprehensive analysis of this approach is presented. It is shown that the Kondo-NCA (KNCA) correctly describes the non-Fermi-liquid fixed point of the multi-channel Kondo effect, similar to the NCA formulation of the multi-channel Anderson model.³⁵ Furthermore, there is quantitative agreement with the Bethe ansatz³⁹ for the temperature and field dependence of the magnetic susceptibility of the isotropic two-channel model. At the same time, the KNCA has several shortcomings, including a spurious ferromagnetic Kondo effect, and an inaccurate exponential dependence of the Kondo temperature on the inverse coupling constants. We are able to pinpoint these shortcomings of the NCA as due to the omission of particle-particle diagrams, which also seems to be the reason for the well-known NCA failure to describe the Fermi-liquid ground state of the single-channel Kondo effect. As a first step towards amending this flaw, an extension of the KNCA is constructed, incorporating particle-particle and particle-hole diagrams on equal footing.

Applying the KNCA to the charge fluctuations in a quantum box with a single-mode junction, we propose an approximate scaling relation for the capacitance line shape as a sharp experimental diagnostic for the low-temperature, non-Fermi-liquid regime of the two-channel Kondo effect. This approximate scaling relation should prove useful in analyzing future experiments, especially on metallic boxes which are more favorable to display a fully developed two-channel Kondo effect.⁴⁰

The remainder of the paper is organized as follows: Section II briefly reviews Matveev's mapping of the charge fluctuations in a single-electron box onto an anisotropic two-channel Kondo Hamiltonian. The KNCA is then presented and analyzed in Sec. III. Technical details of the KNCA and an extended discussion of aspects of this approach not directly related to the Coulomb blockade are deferred to Appendixes A and B. The application of the KNCA to the charge fluctuations at the Coulomb blockade is reported in turn in Sec. IV, followed by a discussion of the main results in Sec. V. Appendix C is devoted an extension of the KNCA that properly preserves particle-hole symmetry.

II. MAPPING THE COULOMB BLOCKADE ONTO AN ANISOTROPIC KONDO PROBLEM

The fundamental connection between the charge fluctuations in a single-electron box at the Coulomb blockade and the Kondo problem was formulated in a key paper by Matveev.²¹ Below we briefly outline Matveev's mapping of the two problems, setting our notations in doing so.

Consider a single-electron box, connected to a lead by a narrow point contact. For a sufficiently narrow point contact, there will be just a single mode weakly connecting the two sides of the constriction. Such a weak link can be described by the tunneling Hamiltonian

$$\mathcal{H}_T = \sum_{kp\sigma} \left\{ t_{kp} c_{k\sigma}^\dagger c_{p\sigma} + h.c. \right\}, \quad (1)$$

where $c_{k\sigma}^\dagger$ ($c_{p\sigma}^\dagger$) creates a conduction electron with spin projection σ in the lead (box), and t_{kp} are the corresponding tunneling matrix elements. To simplify our notations, we use the indices k and p throughout this section to label the single-electron levels in the lead and in the box, respectively. We further assume that the level spacing inside the quantum box is sufficiently small that a continuum-limit description can be used. As recently emphasized by Zaránd *et al.*,⁴⁰ it is difficult to realize this condition in present semiconducting devices, due to the exponentially small many-body energy scale (Kondo temperature) involved. We shall return discuss this assumption later on.

In addition to the tunneling Hamiltonian of Eq. (1), one has the terms describing the isolated lead and box. While the lead can be modeled by a simple noninteracting band with dispersion ϵ_k ,

$$\mathcal{H}_L = \sum_{k\sigma} \epsilon_k c_{k\sigma}^\dagger c_{k\sigma}, \quad (2)$$

for the quantum box one has to consider also the charging energy of the box. Specifically, setting the filled Fermi sea as our reference state and measuring all single-particle energies relative to the Fermi level, the charge inside the box is given by

$$Q = -e \sum_{p\sigma} [c_{p\sigma}^\dagger c_{p\sigma} - \theta(-\epsilon_p)], \quad (3)$$

which has the associated charging energy

$$E_C = \frac{Q^2}{2C_B} + \phi Q. \quad (4)$$

Here C_B is the capacitance of the quantum box, and ϕ is the electrostatic potential in the box measured relative to the lead. The latter is related to the applied gate voltage by some geometric factor. Thus, the full Hamiltonian of the system has the form $\mathcal{H} = \mathcal{H}_L + \mathcal{H}_B + \mathcal{H}_T$, where

$$\mathcal{H}_B = \sum_{p\sigma} \epsilon_p c_{p\sigma}^\dagger c_{p\sigma} + \frac{Q^2}{2C_B} + \phi Q \quad (5)$$

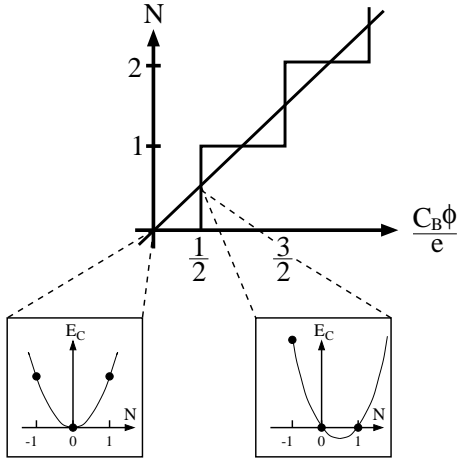


FIG. 1. Zero-temperature charging of the isolated quantum box, in the absence of tunneling to the lead. For a given value of the electrostatic potential ϕ , the charging energy $E_C = (eN)^2/2C_B - e\phi N$ is parabolic in the number of excess electrons in the box, $N = -Q/e$. Each time $\phi C_B/e$ is equal to half an integer, there are two degenerate charge configurations that minimize E_C . This results in abrupt jumps in N each time $\phi C_B/e$ crosses a half-integer value.

describes the isolated single-electron box, which has the single-particle levels ϵ_p .

For zero tunneling and zero temperature, the charge in the quantum box is determined by minimizing E_C with respect to Q . Given the discreteness of the charge, this results in abrupt changes in the ground state of the quantum box each time $\phi C_B/e$ crosses the half-integer value $N + 1/2$, corresponding to the transition from $Q = -eN$ to $Q = -e(N + 1)$ (see Fig. 1). Precisely at $\phi C_B/e = N + 1/2$ the two charge configurations are degenerate, giving rise to strong charge fluctuations in the box.

The effect of weak tunneling is to smear the sharp charge steps at $\phi = e(N + 1/2)/C_B$, yet in a nontrivial manner to be explored below. To this end, let us focus on the vicinity of a particular charge step separating $Q = -eN$ from $Q = -e(N + 1)$. Labeling the deviation from the degeneracy point by $U = \phi - e(N + 1/2)/C_B$, we concentrate on $|U| \ll e/C_B$ and $k_B T \ll e^2/C_B$, such that all charge configurations other than $Q = -eN$ and $Q = -e(N + 1)$ are thermally inaccessible.⁴¹ One can remove all higher energy charge configurations in this case by introducing the operators P_0 and P_1 , which project onto the $Q = -eN$ and $Q = -e(N + 1)$ subspaces, respectively. Omitting a U -independent reference energy, the resulting low-energy Hamiltonian is written as

$$\mathcal{H}_{eff} = \left(\sum_{k\sigma} \epsilon_k c_{k\sigma}^\dagger c_{k\sigma} + \sum_{p\sigma} \epsilon_p c_{p\sigma}^\dagger c_{p\sigma} \right) (P_0 + P_1) + \sum_{kp\sigma} \left\{ t_{kp} P_0 c_{k\sigma}^\dagger c_{p\sigma} P_1 + t_{kp}^* P_1 c_{p\sigma}^\dagger c_{k\sigma} P_0 \right\}$$

$$- \frac{eU}{2} (P_1 - P_0) - eU \left(N + \frac{1}{2} \right) (P_1 + P_0). \quad (6)$$

To illustrate the connection between Eq. (6) and the two-channel Kondo Hamiltonian, it is useful to adopt the following 2×2 matrix representation of the two projection operators:

$$P_0 \longleftrightarrow \begin{pmatrix} 0 & 0 \\ 0 & 1 \end{pmatrix}, \quad P_1 \longleftrightarrow \begin{pmatrix} 1 & 0 \\ 0 & 0 \end{pmatrix}. \quad (7)$$

In addition, we change our notation for the conduction electrons by introducing the isospin label $\alpha = \pm$, distinguishing the quantum-box electrons, $c_{k\sigma\alpha}^\dagger$, from the lead electrons, $c_{k\sigma\alpha}^\dagger$. Neglecting all momentum dependence of the tunneling matrix elements, i.e., taking $t_{kp} = t$, Eq. (6) acquires the form

$$\mathcal{H}_{eff} = \sum_{k\sigma\alpha} \epsilon_{k\alpha} c_{k\sigma\alpha}^\dagger c_{k\sigma\alpha} - eU \left(N + \frac{1}{2} \right) - \frac{eU}{2} \begin{pmatrix} 1 & 0 \\ 0 & -1 \end{pmatrix} + t \sum_{kk'\sigma} \left\{ c_{k\sigma}^\dagger c_{k'\sigma} + \begin{pmatrix} 0 & 1 \\ 0 & 0 \end{pmatrix} + h.c. \right\}. \quad (8)$$

Finally, expressing the 2×2 matrices in terms of a spin- $\frac{1}{2}$ isospin operator \vec{S} , our effective Hamiltonian becomes

$$\mathcal{H}_{eff} = \sum_{k\sigma\alpha} \epsilon_k c_{k\sigma\alpha}^\dagger c_{k\sigma\alpha} - eU S_z - eU (N + 1/2) + \frac{t}{2} \sum_{kk'\sigma\alpha\alpha'} \left\{ c_{k\sigma\alpha}^\dagger \sigma_{\alpha\alpha'}^- c_{k'\sigma\alpha'} S^+ + h.c. \right\}, \quad (9)$$

where $\sigma^\pm = \sigma_x \pm i\sigma_y$ are Pauli matrices. Here we have omitted for convenience the isospin index from the conduction-electron energies in the first term of Eq. (9), which amounts to taking a single joint density of states, $\rho(\epsilon) = \sum_k \delta(\epsilon - \epsilon_k)$, for the quantum box and the lead. Since all quantities related to \vec{S} in the problem depend on the product of the two density of states in the box and in the lead, $\rho(\epsilon)$ is to be understood as the geometric average of the two density of states.⁴²

Up to a constant shift in energy, Eq. (9) is the Hamiltonian of an anisotropic two-channel Kondo impurity in a local magnetic field. Specifically, $J_\perp = 2t$ plays the role of the transverse exchange coupling, while $\mu_B g_J H = eU$ corresponds to an applied magnetic field. The longitudinal exchange coupling in this mapping is set equal to zero. Note that the exchange interaction in Eq. (9) acts on the isospin index, whereas the physical spin is reduced to a passive spectator. Hence the associated many-body screening is that of the charge fluctuations in the quantum box, not that of a physical spin. More specific, the charge in the box is related to the isospin magnetization through

$$\langle Q \rangle = -e \left(N + \frac{1}{2} \right) - e \langle S_z \rangle, \quad (10)$$

while the capacitance of the junction, $C(U, T) = -\partial\langle Q \rangle / \partial U$, is equal to $e^2 / (\mu_B g_J)^2$ times the isospin susceptibility,⁴³

$$\chi(H, T) = \mu_B g_J \frac{\partial \langle S_z \rangle}{\partial H}. \quad (11)$$

As is well known, the low-temperature, low-field properties of the two-channel Kondo Hamiltonian are governed by an intermediate-coupling non-Fermi-liquid fixed point,¹³ which differs markedly from the infinite-coupling fixed point of the single-channel case. In particular, the zero-field susceptibility diverges with decreasing temperature according to $\chi \propto (1/T_K) \log(T_K/T)$, which translates in the present context to an infinite charging slope at $U = 0$ and $T = 0$. T_K in the above expression is the Kondo temperature, which marks the crossover from weak coupling. For the anisotropic Hamiltonian of Eq. (9) it is given by²¹

$$k_B T_K = (D \rho_0 t) \exp \left[-\frac{\pi}{4 \rho_0 t} \right], \quad (12)$$

where $D \sim e^2 / C_B$ is the effective conduction-electron bandwidth, and ρ_0 is the geometric average of the lead and the box density of states at the Fermi level.

Equation (12) is due to Matveev, who studied the Hamiltonian of Eq. (9) within a perturbative renormalization-group approach.²¹ Based on perturbation theory, this approach breaks down as soon as the renormalized exchange couplings are large, limiting its applicability to the weak-coupling regime. Our objective is to develop a quantitative description of all temperature and field regimes, including the low-temperature, non-Fermi-liquid regime. To this end, we first extend the noncrossing approximation to the Kondo Hamiltonian with arbitrary anisotropic spin-exchange couplings.

III. NONCROSSING APPROXIMATION

As mentioned above, to date there is no direct formulation of the NCA for the Kondo-spin Hamiltonian, let alone its strongly anisotropic version of Eq. (9). In fact, previous applications of the NCA to the multi-channel Kondo effect have been restricted to the $SU(N) \times SU(M)$ multi-channel Anderson model.¹³ While the two-channel Anderson model has often been used to model uranium and cerium ions in appropriate crystalline-electric-field environments,¹³ it does not directly apply to the problem at hand, or to any realization of two-level systems in a metal. Furthermore, we note that the anisotropic Kondo Hamiltonian cannot be derived from the Anderson Hamiltonian via the Schrieffer-Wolff transformation,⁴⁴ which illustrates the independence of the two models. Below we extend the formulation of the NCA to the multi-channel Kondo Hamiltonian with arbitrary spin-exchange and potential-scattering couplings.

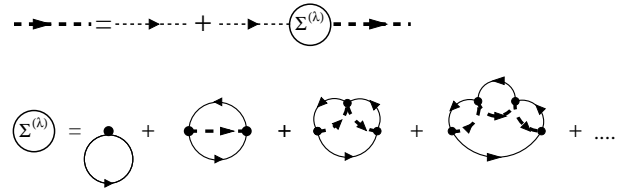


FIG. 2. Diagrammatic representation of the noncrossing approximation for the pseudo-fermion Green function. Here thin (thick) dashed lines represent bare (fully dressed) f Green functions, while full lines stand for bare conduction-electron propagators. In the Coqblin-Schrieffer limit, $J_0 = J_x = J_y = J_z$, these diagrams coincide with the self-consistent ladder approximation of Maekawa *et al.*,³⁸ which can also be derived from the NCA equations for the Anderson impurity model by taking the appropriate Kondo limit.³⁴

As we are interested in devising a general approach, let us consider in this section the fully anisotropic M -channel Kondo Hamiltonian given by

$$\begin{aligned} \mathcal{H} = & \sum_k \sum_{n=1}^M \sum_{\sigma=\uparrow,\downarrow} \epsilon_k c_{kn\sigma}^\dagger c_{kn\sigma} - \mu_B g_J H S_z \\ & + \sum_{\mu=x,y,z} \frac{J_\mu}{2} S_\mu \sum_{n=1}^M \sum_{kk'\sigma\sigma'} \sigma_{\sigma\sigma'}^\mu c_{kn\sigma}^\dagger c_{k'n\sigma'} \\ & + \frac{J_0}{4} \sum_{n=1}^M \sum_{\sigma=\uparrow,\downarrow} \sum_{kk'} c_{kn\sigma}^\dagger c_{k'n\sigma}. \end{aligned} \quad (13)$$

Here, \vec{S} is the impurity spin; σ^μ are Pauli matrices; J_x, J_y , and J_z are independent spin-exchange couplings; $J_0/4$ represents potential scattering at the impurity site; and H is a local applied magnetic field. The Hamiltonian of Eq. (9) corresponds in this notation to $M = 2$, $J_x = J_y = 2t$, $J_z = J_0 = 0$, and $\mu_B g_J H = eU$ [note that σ labels the channel index in Eq. (9), whereas in Eq. (13) it labels the spin index]. The inclusion of potential scattering in Eq. (13) is mainly intended to allow for comparison with the Coqblin-Schrieffer Hamiltonian and the self-consistent ladder approximation of Maekawa *et al.*³⁸ As we shall see, though, its inclusion will provide considerable insight into some of the underlying features of the NCA.

We proceed by introducing Abrikosov's slave-fermion representation,⁴⁵ which generalizes in the Anderson model to the slave-boson representation.⁴⁶ In this representation, one assigns a pseudo fermion to each impurity spin state according to

$$f_\uparrow^\dagger |0\rangle \longleftrightarrow |\uparrow\rangle, \quad f_\downarrow^\dagger |0\rangle \longleftrightarrow |\downarrow\rangle. \quad (14)$$

The physical subspace corresponds to the constraint $\hat{N}_f \equiv \sum_\sigma f_\sigma^\dagger f_\sigma = 1$, which represents the fact that the impurity spin has only two possible states. This constraint distinguishes the pseudo fermions from ordinary fermions.

A convenient way to calculate physical quantities is to work within a grand canonical ensemble with respect to the number of pseudo fermions. These are assigned a chemical potential λ , modifying the Hamiltonian from \mathcal{H} to $\mathcal{H} - \lambda \hat{N}_f$. The projection onto the physical subspace is carried out by taking the limit $\lambda \rightarrow -\infty$. Specifically, physical averages are given by

$$\langle \hat{O} \rangle_{phys} = \frac{1}{Z_{imp}} \lim_{\lambda \rightarrow -\infty} e^{-\beta \lambda} \langle \hat{O} \hat{N}_f \rangle_{\lambda}, \quad (15)$$

where

$$Z_{imp} = \lim_{\lambda \rightarrow -\infty} e^{-\beta \lambda} \langle \hat{N}_f \rangle_{\lambda} \quad (16)$$

is the ‘‘impurity contribution’’ to the partition function. Here subscripts λ denote averages within the grand-canonical ensemble. In practice, one can drop the \hat{N}_f operator in Eq. (15) for those physical operators \hat{O} that give zero when acting on the $\hat{N}_f = 0$ subspace, which greatly simplifies the calculations.

A central quantity in the calculation of physical observables is the pseudo-fermion Green function, $G_{\sigma}^{(\lambda)}(z)$, which enters in its projected form $G_{\sigma}(z) = \lim_{\lambda \rightarrow -\infty} G_{\sigma}^{(\lambda)}(z - \lambda)$. The latter will be referred to hereafter as the pseudo-fermion Green function.⁴⁷ The pseudo-fermion Green function takes the standard form $G_{\sigma}(z) = [z - \epsilon_{\sigma} - \Sigma_{\sigma}(z)]^{-1}$, where $\Sigma_{\sigma}(z)$ is the projected self-energy, and $\epsilon_{\sigma} = -\sigma \frac{1}{2} \mu_B g_J H$ is the bare energy of the impurity spin (we use $\sigma = \uparrow, \downarrow$ and $\sigma = \pm$ interchangeably to label the spin z component). The Kondo-NCA (KNCA) is defined by a particular set of self-energy diagrams, shown in Fig. 2. Although additional diagrams without any crossings do exist for the Kondo-spin Hamiltonian (specifically the particle-particle ladder, see Appendix C), we refer to this approximate scheme as the NCA, because it has the same general structure as that of the conventional NCA for the Anderson Hamiltonian.

Working within the slave-fermion representation, we write the interaction term of Eq. (13) in the form

$$\sum_{n=1}^M \sum_{kk'} \sum_{\alpha\beta\alpha'\beta'} V_{(\alpha\beta)(\alpha'\beta')} c_{nk\alpha}^{\dagger} c_{nk'\alpha'} f_{\beta'}^{\dagger} f_{\beta}, \quad (17)$$

where

$$V_{(\alpha\beta)(\alpha'\beta')} = \sum_{\mu=0,x,y,z} \frac{J_{\mu}}{4} \sigma_{\alpha\alpha'}^{\mu} \sigma_{\beta'\beta}^{\mu}. \quad (18)$$

Here σ^0 denotes the 2×2 unity matrix. Viewing the $V_{(\alpha\beta)(\alpha'\beta')}$ coefficients as the elements of a 4×4 matrix, this choice of labels allows for a convenient summation of the ladder diagram of Fig. 2. Details of the derivation are provided in Appendix A. For a zero magnetic field, when both spin orientations are equivalent, one obtains⁴⁸

$$\Sigma(\epsilon + i\delta) = \frac{M}{2} \sum_k f(-\epsilon_k) \Delta(\epsilon - \epsilon_k + i\delta), \quad (19)$$

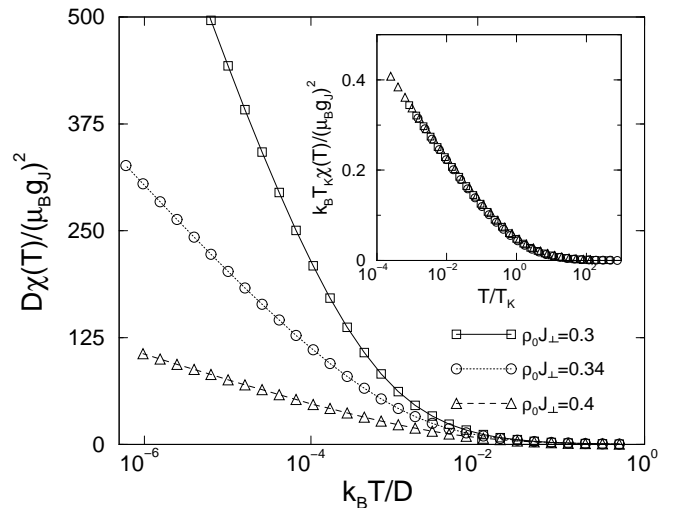


FIG. 3. KNCA results for the zero-field magnetic susceptibility of the anisotropic two-channel Kondo impurity with $J_z = 0$ and different $\rho_0 J_{\perp}$. Here and throughout the paper we use a semi-circular conduction-electron density of states with half-width D . At low temperatures, $\chi(T)$ diverges logarithmically with decreasing temperature, in accordance with exact results. The robustness and universality of the logarithmic temperature dependence is demonstrated in the inset, where all lines have been collapsed onto a single curve by rescaling $\chi(T)$ and T with the Kondo temperature, T_K . The latter is extracted according to Eq. (24), taking the values $k_B T_K/D = 4 \times 10^{-4}$, 1.15×10^{-3} , and 3.85×10^{-3} for $\rho_0 J_{\perp} = 0.3$, 0.34 , and 0.4 , respectively.

where

$$\Delta(\epsilon + i\delta) = - \sum_{\mu=0,x,y,z} \frac{A_{\mu}}{1 - A_{\mu} \Pi(\epsilon + i\delta)}, \quad (20)$$

$$\Pi(\epsilon + i\delta) = - \sum_k f(\epsilon_k) G(\epsilon + \epsilon_k + i\delta). \quad (21)$$

Here $f(\epsilon)$ is the Fermi-Dirac distribution function, and the A_{μ} coefficients are defined as

$$A_0 = \frac{1}{4} (J_0 + J_x + J_y + J_z), \quad (22)$$

$$A_i = \frac{1}{4} (J_0 + 2J_i - J_x - J_y - J_z) \quad (23)$$

($i = x, y, z$). For $J_0 = J_x = J_y = J_z$, corresponding to the Coqblin-Schrieffer Hamiltonian, Eqs. (19)–(21) coincide with the self-consistent ladder approximation of Maekawa *et al.*³⁸

As stated above, Eqs. (19)–(21) are for a zero magnetic field. However, to study the smearing of the charge step for the quantum box, it is necessary to include also a local magnetic field. The addition of a finite magnetic field clearly distinguishes the present NCA formulation from those of the Anderson³⁴ and Coqblin-Schrieffer³⁸

Hamiltonians. While in the latter two cases one simply replaces the zero-field pseudo-fermion propagators entering the NCA equations with spin-dependent ones, the structure of Eqs. (19)–(21) is substantially modified once H is nonzero. The generalization of Eqs. (19)–(21) to a nonzero field is specified in Appendix A, Eqs. (A4), (A6), and (A7).

Although somewhat cumbersome, the magnetic-field equations are essential to our discussion. They are solved numerically by iterations similar to the zero-field ones. From their solution one can compute the field-dependent magnetization $M(H, T)$, from which $\chi(H, T)$ follows by direct numerical differentiation with respect to H . Interestingly, we found it advantageous to use this finite-field differentiation procedure also when computing the zero-field susceptibility. This somewhat surprising result stems from the fact that the standard magnetization bubble acquires a nontrivial vertex correction that is absent for both the Anderson and Coqblin-Schrieffer Hamiltonians, and which contributes an important $\log-T$ diverging term to the low-temperature susceptibility of the two-channel case (see Appendix A, Figs. 10 and 11). Deferring all details of the numerical procedure to Appendix A, below we summarize the main features of the KNCA approach. All results presented below were obtained for a semi-circular conduction-electron density of states with half-width D : $\rho(\epsilon) = \rho_0 \sqrt{1 - (\epsilon/D)^2}$, where ρ_0 is the conduction-electron density of states at the Fermi level.

The KNCA approach presented above has several notable successes. Taking the zero-temperature limit and performing a Müller-Hartmann⁴⁹ type of analysis, one can show that Eqs. (19)–(21) reproduce the exact critical exponents of the multi-channel ($M > 1$) Kondo effect for antiferromagnetic couplings, similar to the NCA treatment of the multi-channel Anderson model.³⁵ Focusing on antiferromagnetic couplings, the low-temperature susceptibility for the $M = 2$, two-channel case diverges logarithmically with decreasing temperature, in accordance with exact results.¹³ For the anisotropic limit of Eq. (9), this is demonstrated in Fig. 3, for different values of $\rho_0 J_\perp$ (J_\perp being the transverse spin-exchange coupling; $J_\perp \equiv J_x = J_y$). Most significantly, there is quantitative agreement with the Bethe ansatz for the field and temperature dependence of the susceptibility in the isotropic limit,³⁹ as shown in Fig. 4. Here and throughout the paper we extract the two-channel Kondo temperature from the Bethe ansatz expression for the slope of the $\log-T$ diverging term in the zero-field susceptibility:⁵⁰

$$\chi(T) \sim \frac{(\mu_B g J)^2}{20 k_B T_K} \ln(T_K/T). \quad (24)$$

Hence the KNCA correctly describes the non-Fermi-liquid fixed point of the multi-channel Kondo effect both qualitatively and quantitatively. Finally, Eqs. (19)–(21) correctly give rise to a quantum phase boundary between “antiferromagnetic” ($J_z > -|J_\perp|$) and “ferromagnetic” ($J_z \leq -|J_\perp|$) couplings, each of which is characterized by different threshold exponents.^{49,51}

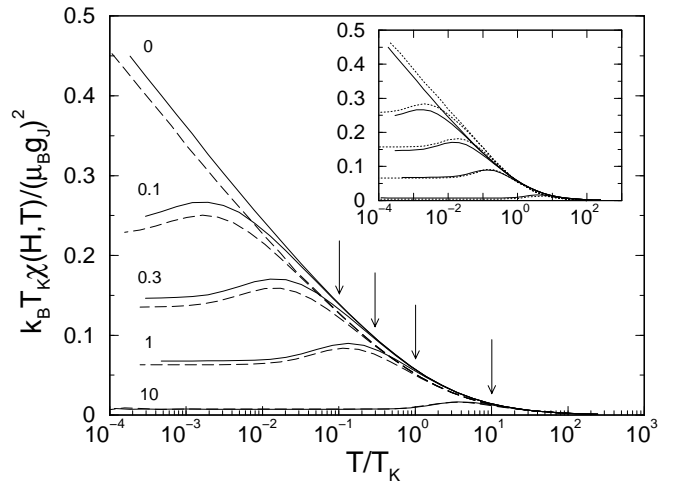


FIG. 4. Temperature and field dependence of the magnetic susceptibility within the KNCA: full lines are for the isotropic two-channel Kondo model with $J_0 = 0$ and $\rho_0 J = 0.2667$ ($k_B T_K/D = 2 \times 10^{-3}$); dashed lines are for the anisotropic two-channel Kondo model with $J_0 = J_z = 0$ and $\rho_0 J_\perp = 0.4$ ($k_B T_K/D = 3.85 \times 10^{-3}$). The applied magnetic field takes the values of $\mu_B g J H/k_B T_K = 0, 0.1, 0.3, 1$, and 10 , according to the labels marking each set of curves. For each field, the associated temperature $T = \mu_B g J H/k_B$ is indicated by an arrow. Inset: Comparison between the Bethe ansatz (dotted lines, taken from Ref. 39) and the KNCA (full lines), for the isotropic two-channel Kondo model. Here $\rho_0 J = 0.2667$ for the KNCA curves. The values of $\mu_B g J H/k_B T_K$ used and their line assignments are identical to those in the main figure.

At the same time, Eqs. (19)–(21) have several clear shortcomings: (i) A spurious Kondo-type effect (i.e., a low-temperature resonance with an underlying nonperturbative energy scale) is found for ferromagnetic couplings, albeit with different characteristic exponents than in the antiferromagnetic case. For $J_0 > 0$, this spurious Kondo-type effect extends also to pure potential scattering; (ii) Starting from a particle-hole symmetric Hamiltonian, the KNCA breaks particle-hole symmetry, which is manifest, for example, in the asymmetric energy dependence of the conduction-electron T -matrix [See Appendix A, Fig. 12]; (iii) Inaccuracies are found in the exponential dependence of Kondo temperature on the inverse coupling constants. Specifically, the exponential dependence of T_K on $1/J_\mu$ can be estimated from the location of the lowest pole in the first iteration for $\Delta(\epsilon)$ at zero temperature. Subsequent iterations only modify the pre-exponential factor. For antiferromagnetic couplings with $J_\perp > 0$ one thus obtains

$$T_K^{(NCA)} \sim D \exp \left[-\frac{1}{\rho_0 A_0} \right], \quad (25)$$

which reduces in the isotropic case [when $A_0 = 3\rho_0 J/4$, see Eq. (22)] to $T_K^{(NCA)} \sim D \exp[-4/3\rho_0 J]$. Here D is the conduction-electron bandwidth. This should to be con-

trusted with the well-known result $T_K \sim D \exp[-1/\rho_0 J]$, valid for any number of channels M .⁵² Similarly, for the anisotropic Hamiltonian of Eq. (9) one obtains $T_K^{(NCA)} \sim D \exp[-2/\rho_0 J_\perp]$, compared to $T_K \sim D \exp[-\pi/2\rho_0 J_\perp]$ of Eq. (12). Only in the Coqblin-Schrieffer limit, when a nonzero potential scattering $J_0 = J$ is included, does one recover the correct exponential dependence of T_K on $1/J$ for isotropic spin-exchange couplings.

As discussed at length in Appendix B, we are able to pinpoint these shortcomings of the NCA as due to the omission of particle-particle diagrams. While particle-particle diagrams are of higher order in $1/N$ in a formal large- N expansion as per the Anderson Hamiltonian,³⁴ they must be treated on equal footing in the spin- $\frac{1}{2}$ Kondo model. The omission of particle-particle diagrams leads to the spontaneous generation of potential scattering, drives the system to a ferromagnetic Kondo effect, and spoils the exponential dependence of the Kondo temperature on the inverse coupling constants. It is our belief that their omission is also responsible for the well-known NCA failure to describe the Fermi-liquid ground state of the single-channel Kondo effect. We expand on these ideas in Appendix C, where an extension of the KNCA scheme is proposed based on a summation of all parquet diagrams. It is shown that even the crudest treatment of the extended scheme gives encouraging results for the amendment of the above NCA flaws.

It is important to note, though, that since T_K is exponentially sensitive to the microscopic parameters of the system, it is best extracted directly from the experiment. Thus, viewing T_K as an experimental parameter, one can use the KNCA to reliably study the delicate interplay between the temperature T , the local magnetic field H , and the Kondo temperature T_K in the non-Fermi-liquid regime of the two-channel Kondo effect.

IV. APPLICATION OF THE KNCA TO THE COULOMB BLOCKADE

In this section, we apply the KNCA to study the smearing of the charge step for a quantum box, in the case of a narrow point contact. Smearing of the charge step was previously studied by various authors using different approaches. These include renormalization-group techniques,²¹ perturbation theory in the tunneling conductance,⁵³ infinite summations of subclasses of diagrams,^{54,55} and Monte Carlo simulations.⁵⁶ However, these approaches generally fail at low temperatures near the degeneracy point. Here we exploit the KNCA to reliably study this regime for a single-mode junction.

As discussed in Sec. II, the excess charge in the quantum box is related within the two-channel Kondo mapping to the isospin magnetization [see Eq. (10)], while the capacitance corresponds to the isospin susceptibility. Our task therefore amounts to computing the field and temperature dependence of the magnetization and sus-

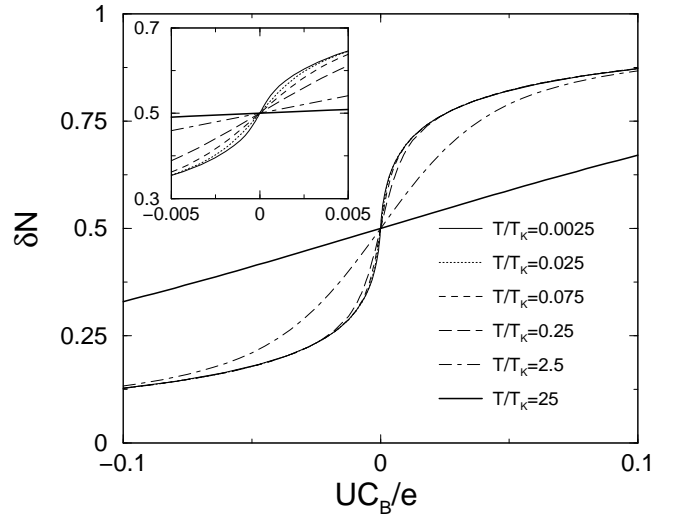


FIG. 5. Temperature dependence of the charge step between the $\langle Q \rangle = -eN$ and $\langle Q \rangle = -e(N+1)$ charge plateaus, as obtained from the KNCA. Here we parameterize the transition between the plateaus by $\delta N = -\langle Q \rangle/e - N$. The tunneling matrix element is taken to be $\rho_0 t = 0.2$, corresponding to $\rho_0 J_\perp = 0.4$ in the anisotropic two-channel Kondo representation of Eq. (13). The corresponding Kondo temperature is equal to $k_B T_K/D = 3.85 \times 10^{-3}$. Following Matveev,²¹ we identify the conduction-electron bandwidth D with e^2/C_B , such that eU/D is equal to UC_B/e . The overall shape of the charge step is mostly unchanged for $T \ll T_K$, however the slope around $U = 0$ continues to steepen with decreasing temperature (see inset). Eventually, an infinite slope develops at $U = 0$ as $T \rightarrow 0$.

ceptibility of the anisotropic two-channel Kondo Hamiltonian with $J_z = 0$.

A. Evolution of the charge step

Generally speaking, there are three energy scales that govern the shape of the charge step for the quantum box: $k_B T$, $k_B T_K$, and e^2/C_B . At high temperatures, $k_B T \gg e^2/C_B$, the classical picture is recovered. Thermal fluctuations are sufficiently strong to wash out the Coulomb blockade, and a linear Q vs. ϕ curve is obtained with a slope of C_B . The Coulomb-blockade picture emerges as $k_B T$ is lowered below e^2/C_B . Specifically, for $k_B T \ll e^2/C_B$ there are extended, nearly horizontal charge plateaus, separated by rather narrow charge steps. The charge plateaus extend over a length of $\Delta(eU)_{\text{plateau}} \approx e/C_B$, while the charge steps are confined to a width of $\Delta(eU)_{\text{step}} \propto \max\{k_B T, k_B T_K\}$.⁵⁷ It is only in this temperature regime and in the vicinity of the charge steps that the mapping onto the Hamiltonian of Eq. (9) applies.

Restricting attention to $k_B T \ll e^2/C_B$, Fig. 5 depicts the evolution of the charge step with decreasing T/T_K . For $T_K \ll T$, the charge step is governed by thermal

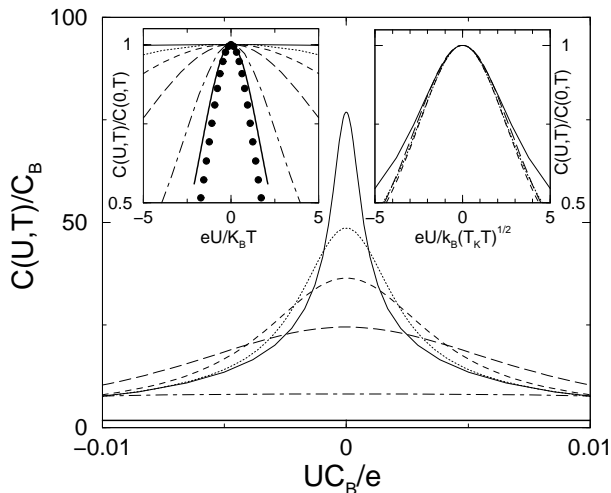


FIG. 6. Temperature dependence of the capacitance line shape $C(U, T)$. Here the temperatures and line-type assignments are the same as in Fig. 5. With decreasing temperature, $C(U, T)$ develops a sharp peak about the center of the charge step ($U = 0$), the height of which diverges logarithmically with decreasing T . Left inset: The reduced capacitance, $C(U, T)/C(0, T)$, plotted versus $x_1 = eU/k_B T$. With increasing temperature, the curves approach the shape of the derivative of the Fermi-Dirac distribution function, normalized to unity peak height [i.e., $4e^{x_1}/(1 + e^{x_1})^2$, full circles]. Right inset: $C(U, T)/C(0, T)$ plotted versus $x_2 = eU/k_B \sqrt{T T_K}$, for the four temperatures below T_K (i.e., $T/T_K = 0.0025, 0.025, 0.075$, and 0.25). For small to intermediate x_2 , all lines approximately collapse onto a single curve.

fluctuations. This is best seen in the capacitance line shape, which approaches the shape of the derivative of the Fermi-Dirac distribution function for elevated temperatures (see Fig. 6, left inset). For $T_K \ll T$, the width and shape of the charge step are therefore set by the temperature. By contrast, quantum fluctuations dominate for $T \ll T_K$. The overall extent of the step is proportional to $k_B T_K$, and its shape is mostly the same as at $T = 0$. Note, however, that the slope at $U = 0$ continues to steepen with decreasing temperature (see inset of Fig. 5), approaching an infinite slope as $T \rightarrow 0$.²¹ This lack of saturation in the capacitance at $U = 0$ corresponds to the divergence of the linear susceptibility within the two-channel Kondo model, which is a hallmark of the non-Fermi-liquid ground state that develops in this case.

The evolution of the charge step is best resolved in the capacitance line shape $C(U, T)$, shown in Fig. 6. When plotted as a function of UC_B/e (corresponding to eU/D with $D = e^2/C_B$), the capacitance develops a sharp peak about the center of the charge step ($U = 0$), the height of which diverges logarithmically with decreasing T . To maintain a total integrated weight of one unit charge, there is a redistribution of weight from the shoulders of the peak to its center as T is decreased.

The crossover from thermal fluctuations to quantum fluctuations can be quantified by considering the reduced capacitance, $C(U, T)/C(0, T)$. To this end, we have plotted the reduced capacitance of Fig. 6 once versus $x_1 = eU/k_B T$ (left inset), and once versus $x_2 = eU/k_B \sqrt{T_K T}$ (right inset). Clearly, two different qualitative behaviors are found, depending on whether $T \gg T_K$ or $T \ll T_K$. For $T \gg T_K$, the reduced capacitance approaches the curve $4e^{x_1}/(1 + e^{x_1})^2$, which is just the derivative of the Fermi-Dirac distribution function, normalized to unity peak height. This is to be expected of thermal fluctuations, when the occupations of the two available charge configurations in the quantum box follow the Fermi-Dirac distribution function. A different qualitative behavior is seen for $T \ll T_K$. Here there is a strong fanning out of the reduced capacitance when plotted versus x_1 , but an apparent scaling when plotted versus x_2 . As argued below, this approximate scaling with x_2 is an important characteristic of the non-Fermi-liquid regime of the two-channel Kondo effect.

B. Approximate scaling with U/\sqrt{T}

To understand the apparent scaling of U with \sqrt{T} for $T \ll T_K$, we go back to the two-channel Kondo representation of the Coulomb blockade. As is well known, the intermediate-coupling non-Fermi-liquid fixed point of the two-channel Kondo model is unstable against an applied magnetic field, which drives the system to a phase-shifted Fermi-liquid ground state.⁵⁸ For a weak magnetic field, $\mu_B g_J |H| \ll T_K$, this crossover from non-Fermi-liquid to Fermi-liquid behavior is associated with an energy scale

$$k_B T_x = \frac{(\mu_B g_J H)^2}{k_B T_K}, \quad (26)$$

that depends quadratically on H . Loosely speaking, for $T_x \ll T \ll T_K$ a magnetic field has only a minor effect on the low-temperature thermodynamics, while for $T \ll T_x \ll T_K$ the effect of a temperature is small. In particular, the susceptibility $\chi(H, T)$ is weakly field dependent for $T_x \ll T$, and is logarithmically field dependent for $T \ll T_x$. The connection with the reduced-capacitance plot of Fig. 6 is made by recalling that eU and $C(U, T)/C(0, T)$ in the Coulomb blockade map onto $\mu_B g_J H$ and $\chi(H, T)/\chi(0, T)$, respectively, in the two-channel Kondo representation. Thus, when plotted versus $x_2 = \pm \sqrt{T_x/T}$, the reduced capacitance shows a characteristic crossover from approximately one for $|x_2| < 1$, to logarithmic in $|x_2|$ for $|x_2| > 1$.

Although the right inset of Fig. 6 seems to suggest an exact scaling form for the reduced capacitance as a function of x_2 for $T \ll T_K$, we emphasize that this scaling is only approximate. Namely, writing the reduced capacitance in the form

$$F(x_2, T) = C(U, T)/C(0, T) \quad (27)$$

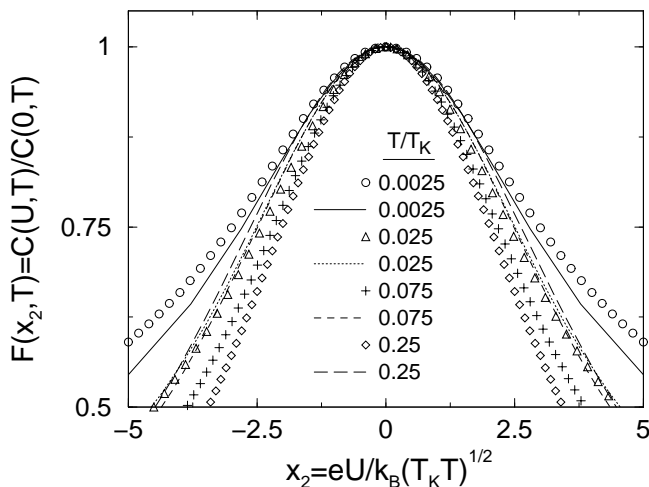


FIG. 7. Comparison of the proposed scaling function $F(x_2, T)$ at the Emery-Kivelson point with the one obtained at the Coulomb blockade using the KNCA (curves taken from the right inset of Fig. 6). Here symbols correspond to the Emery-Kivelson point, while lines mark the curves of the KNCA. Note that T is varied over two decades of temperature, from $T/T_K = 0.25$ down to $T/T_K = 0.0025$.

with $x_2 = eU/k_B\sqrt{T_K T}$, F does not reduce in the limit $T \ll T_K$ to a function of x_2 alone. Nevertheless, the residual T dependence is logarithmic in nature (see below), and therefore relatively weak.

So far our discussion has been limited to the KNCA, and to the $J_z = 0$ limit of the anisotropic two-channel Kondo model. However, we expect the approximate scaling function of Eq. (27) to be generic to all antiferromagnetic couplings of the anisotropic two-channel Kondo Hamiltonian. To support this conjecture and to gain analytical insight into the structure of $F(x_2, T)$, we consider below the opposite limit of $J_z \gg J_\perp$, for which an exact analytic solution of the two-channel Kondo model exists for a particular value of J_z . At this special point, known as the Emery-Kivelson point,⁵⁹ one can compute $F(x_2, T)$ exactly, without resorting to the KNCA. The results for this special limit are summarized in Fig. 7 and Eqs. (31)–(33) below.

C. Comparison with the Emery-Kivelson point

As noted by Emery and Kivelson,⁵⁹ the two-channel Kondo model with $\rho_0 J_\perp \ll \rho_0 J_z = 1$ ($J_z = \pi v_F$ in the notations of Ref. 59) can be mapped exactly onto a noninteracting “Majorana” resonant-level model, which is the analog of the Toulouse limit for the single-channel case.⁶⁰ At this special point, one has an exact analytic solution of the anisotropic two-channel Kondo model, which captures the essential low-temperature physics of the model. In particular, one can use the Emery-Kivelson point to extract universal low-temperature behaviors of the two-

channel Kondo model.⁶¹

Using the exact solution of Emery and Kivelson, we computed the local-field and temperature dependence of the magnetization at the solvable point. The resulting expression reads

$$M(H, T) = \frac{(\mu_B g_J)^2 H}{20 T_K} \operatorname{Re} \left\{ \frac{\psi(z_+) - \psi(z_-)}{\Delta} \right\}, \quad (28)$$

where $\psi(z)$ is the digamma function,⁶² z_\pm are equal to

$$z_\pm = \frac{1}{2} + \frac{5 T_K}{\pi^2 T} (1 \pm \Delta), \quad (29)$$

and Δ is given by

$$\Delta = \sqrt{1 - \left(\frac{\pi \mu_B g_J H}{10 T_K} \right)^2}. \quad (30)$$

Here T_K is the Kondo temperature, defined according to the Bethe ansatz expression for the slope of the log- T diverging term in the zero-field susceptibility, Eq. (24). With this definition, T_K is related to the half-width Γ of the Majorana resonant level (see Ref. 59) through $T_K = \pi \Gamma / 20$. The field-dependent susceptibility $\chi(H, T)$ is readily obtained from Eq. (28) by differentiating $M(H, T)$ with respect to H .

Focusing on $T < T_K$ and substituting $C(U, T)/C(0, T)$ and eU for $\chi(H, T)/\chi(0, T)$ and $\mu_B g_J H$, respectively, Fig. 7 compares the proposed scaling function $F(x_2, T)$ at the solvable point with the one obtained within the KNCA for the Coulomb blockade. There is good overall agreement between the two cases, even though one is dealing with two opposite limits of the anisotropic two-channel Kondo model, and with two entirely different methods of calculation (KNCA versus an exact solution based on mapping onto a “Majorana” resonant-level model). Although the residual T dependence is more pronounced at solvable point, it is still quite small considering that T is varied in Fig. 7 over two decades of temperature.

The great advantage of the solvable point, though, lies in the explicit form of $F(x_2, T)$, which allows for an analytic study of the limit $k_B T, e|U| \ll k_B T_K$. Explicitly, omitting terms that are either a factor of $\mathcal{O}((eU/T_K)^2)$ or a factor of $\mathcal{O}(T/T_K)$ smaller than the leading-order ones, $F(x_2, T)$ is expressed as

$$F(x_2, T) = 1 - \frac{g(x_2)}{h(T)}, \quad (31)$$

where

$$g(x_2) = \psi\left(\frac{1}{2} + \frac{x_2^2}{40}\right) + \frac{x_2^2}{20} \psi^{(1)}\left(\frac{1}{2} + \frac{x_2^2}{40}\right) - \psi\left(\frac{1}{2}\right) \quad (32)$$

and

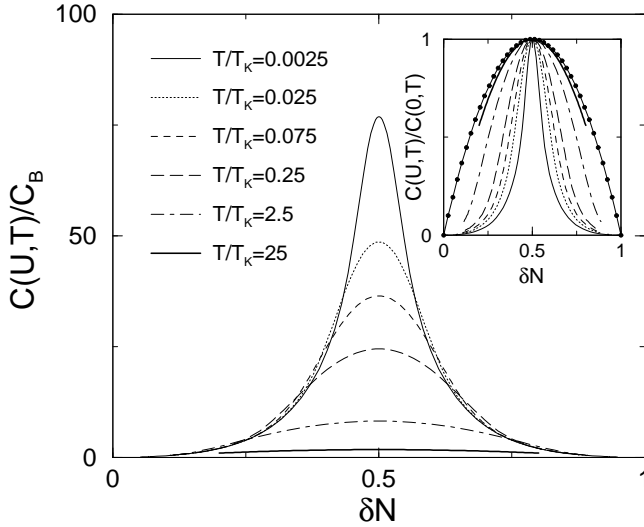


FIG. 8. The capacitance line shapes of Fig. 6, re-plotted as a function of $\delta N = -\langle Q \rangle/e - N$. Within the two-channel Kondo representation, this corresponds to plotting the magnetic susceptibility as a function of the magnetization. For $T < T_K$, there are strong deviations from the parabolic form of Eq. (34), which characterizes pure thermal fluctuations. Inset: A plot of the reduced capacitance $C(U, T)/C(0, T)$ versus δN . In accordance with predominant thermal fluctuations, for $T \gg T_K$ the reduced capacitance approaches the parabola $4\delta N(1 - \delta N)$ (line with full circles).

$$h(T) = \psi\left(\frac{1}{2} + \frac{10T_K}{\pi^2 T}\right) - \psi\left(\frac{1}{2}\right) \approx \log\left(\frac{7.2T_K}{T}\right). \quad (33)$$

Here $\psi^{(1)}(z) = d\psi/dz$ is the trigamma function,⁶² while $g(x_2) \approx 3\pi^2 x_2^2/80$ for $|x_2| \ll 1$. Clearly, T enters $F(x_2, T)$ only logarithmically through $h(T)$, which explains the rather weak temperature dependence of the proposed scaling function. We are therefore led to conclude that a scaling plot of the reduced capacitance versus $x_2 = eU/k_B\sqrt{T_K T}$ provides a sharp diagnostic for the two-channel Kondo scenario, directly testing the associated non-Fermi-liquid scaling of U with \sqrt{T} at low temperatures.

D. Capacitance versus average charge

Finally, a different manifestation of the onset of quantum fluctuations is provided by the inter-relation between the capacitance line shape and the average charge in the quantum box. Specifically, in Fig. 8 we have re-plotted the capacitance line shape of Fig. 6 as a function of the average number of excess electrons in the box, parameterized by $\delta N = -\langle Q \rangle/e - N$. Within the two-channel Kondo representation, this corresponds to plotting the magnetic susceptibility as a function of the magnetization. In the case of pure thermal fluctuations, when

$\delta N = 1 - f(eU)$ follows the Fermi-Dirac distribution function, one has the standard relation

$$C(U, T) = \frac{e^2}{k_B T} \delta N(1 - \delta N). \quad (34)$$

Here we have assumed that $k_B T, e|U| \ll e^2/C_B$, such that all higher energy charge configurations can be neglected. Thus, up to a prefactor of $1/T$, $C(U, T)$ displays a universal parabolic dependence on δN . The onset of quantum fluctuations is reflected in the breakdown of the above parabolic form.

As seen in Fig. 8, for $T \gg T_K$ the capacitance line shape approaches the parabolic form of Eq. (34), in accordance with predominant thermal fluctuations. By contrast, for $T < T_K$ there are strong deviations from the parabolic form of Eq. (34). Specifically, the capacitance line shape is much narrower than that of Eq. (34), with concave shoulders that saturate with decreasing temperature. This is most clearly seen in the inset of Fig. 8, where the reduced capacitance is plotted versus δN .

V. DISCUSSION

In this paper, we have extended the NCA to the Kondo-spin Hamiltonian with arbitrary spin-exchange and potential-scattering couplings, and applied it to the charge fluctuations in a single-electron box at the Coulomb blockade. The KNCA correctly describes the non-Fermi-liquid fixed point of the multi-channel Kondo effect both qualitatively and quantitatively. It reproduces the exact non-Fermi-liquid exponents and logarithms of the multi-channel Kondo effect, and gives surprisingly accurate results for the temperature and field dependence of the magnetic susceptibility in the isotropic two-channel case (see Fig. 4). Hence the KNCA offers a reliable approach to study the delicate interplay between the temperature T , the local magnetic field H , and the Kondo temperature T_K in the non-Fermi-liquid regime of the two-channel Kondo effect.

At the same time, the KNCA reveals several shortcomings of the NCA that are not apparent from the more common applications of this approach to the multi-channel Anderson and Coqblin-Schrieffer Hamiltonians:

1. *Kondo temperature* — For general antiferromagnetic couplings, the NCA class of diagrams is insufficient for producing the correct exponential dependence of T_K on the inverse coupling constants. In fact, for an isotropic spin-exchange interaction J , the correct exponential dependence of T_K on $1/J$ is recovered only if a matching potential-scattering term of magnitude $J_0 = J$ is included. Interestingly, this is precisely the case corresponding to the Anderson and Coqblin-Schrieffer Hamiltonians. That J_0 enters the exponential dependence of T_K is an artifact of the KNCA, as is the fact that $J_0 = J$ is required in order to recover the correct exponential dependence of T_K on $1/J$.

2. *Particle-hole symmetry* — The NCA inherently breaks particle-hole symmetry. Starting from a particle-hole symmetric Hamiltonian, the KNCA violates particle-hole symmetry, which is most clearly manifest in the asymmetric energy dependence of the conduction-electron T -matrix. We note that a similar asymmetry in the shape of the Kondo resonance was also found for the multi-channel Anderson model, where it was attributed to the lack of an underlying particle-hole symmetry.³⁵ From the KNCA we conclude that such an asymmetry in the Kondo resonance is an inherent feature of the NCA, independent of whether the underlying Hamiltonian is particle-hole symmetric or not.

3. *Ferromagnetic Kondo effect* — One regime obviously not accessible starting from an Anderson Hamiltonian is that of ferromagnetic spin-exchange couplings. For ferromagnetic couplings, the KNCA produces a spurious Kondo-type effect, which extends to pure potential scattering if $J_0 > 0$.

As discussed in detail in Appendix B, all the above deficiencies of the KNCA are a consequence of the omission of particle-particle diagrams, which must be treated on equal footing for the spin- $\frac{1}{2}$ Kondo model. To this end, an extended scheme was devised in Appendix C, based on a complete summation of all parquet diagrams. Preliminary studies of the extended scheme seem to suggest the amendment of the above NCA flaws. We further expect it to remedy the well-known NCA failure to describe the Fermi-liquid ground state of the single-channel Kondo effect, much in the same way as the conserving T -matrix approach does for the Anderson model.⁶³ Although we anticipate an intimate relation between our extended scheme and the conserving T -matrix approach of Kroha *et al.*,⁶³ we are unable to establish any formal linkage between the two approaches.

Applying the KNCA to the charge fluctuations in a single-electron box at the Coulomb blockade, two approaches have been proposed to quantify the crossover from thermal fluctuations to quantum fluctuations in the case of a narrow point contact: (i) By plotting the reduced capacitance $C(U, T)/C(0, T)$ versus appropriate scaling combinations of the electrostatic potential U and the temperature T ; and (ii) By plotting the reduced capacitance versus the average number of excess electrons in the quantum box, δN . In the latter case, pure thermal fluctuations are characterized by a universal parabolic form, which breaks down as soon as the temperature is lowered down to T_K . In the former case, different scalings of U with T characterize the high-temperature (thermal fluctuations) and the low-temperature (quantum fluctuations) regimes. As seen in Fig. 6, for $e^2/C_B \gg T \gg T_K$ the reduced capacitance approaches a universal function of $x_1 = eU/k_B T$, corresponding to the derivative of the Fermi-Dirac distribution function. By contrast, for $T_K \gg T$ there is an approximate scaling with $x_2 = eU/k_B \sqrt{T_K T}$, which differs markedly from both thermal fluctuations and ordinary lifetime broadening.

This unusual scaling of U with \sqrt{T} for $T \ll T_K$ is a dis-

tinct characteristic of the non-Fermi-liquid regime of the two-channel Kondo effect. It directly probes the anomalous one-half scaling dimension of an applied magnetic field near the intermediate-coupling fixed point of the two-channel model. Although the reduced capacitance does not show exact scaling with x_2 , the residual temperature dependence is logarithmic in nature, and thus sufficiently weak to render a scaling plot of $C(U, T)/C(0, T)$ versus U/\sqrt{T} a sharp experimental diagnostic for the observation of the two-channel Kondo scenario. For example, by plotting the reduced capacitance versus U/\sqrt{T} for two temperatures differing by a factor of two or more, one should be able to distinguish whether the relevant scaling variable is U/\sqrt{T} or not. The sole requirement is that both temperatures be lower than T_K , which itself may be extracted from the shape of the scaling curve. Moreover, the proposed scaling relation should equally apply to the case of nearly perfect transmission, which likewise corresponds to the two-channel Kondo effect.²²

A few words are in order at this point about the experimental feasibility of reaching the low-temperature, non-Fermi-liquid regime of the two-channel Kondo effect. There are two main limiting factors for observing a fully developed two-channel Kondo effect: (i) The charging energy, e^2/C_B , must be sufficiently large in order for a measurable Kondo temperature to emerge; (ii) The mean level spacing in the quantum box must be sufficiently small as not to cut off the two-channel Kondo effect. These two conditions set opposite limitations on the size of the quantum box, which cannot be too large nor too small. As recently pointed out by Zaránd *et al.*,⁴⁰ it is practically impossible to meet both conditions in present semiconducting devices, but these conditions can be fulfilled in metallic quantum boxes. The main complication with metallic devices has to do with the construction of atomic-size junctions, which are required for obtaining single-mode junctions. The latter are needed since the relevant energy scale for the onset of the two-channel Kondo effect decreases exponentially with the number of tunneling modes.⁴⁰

Finally, we wish to mention several potential applications of the KNCA, beyond the present study of the charge fluctuations in a quantum box. The most natural, perhaps, is the application of the KNCA to the nonequilibrium scattering off nonmagnetic two-level tunneling systems.^{14–16} Previous efforts in this direction have focused on the two-channel Anderson model,¹⁷ which has no direct microscopic justification for TLS. The KNCA allows one to study the actual anisotropic Kondo model appropriate for this case. It would be particularly interesting to see whether there are any quantitative changes to the scaling curves for the differential conductance with $eV/k_B T$ upon going from the two-channel Anderson model to the anisotropic two-channel Kondo model.

Another interesting possibility is the extension of the present work to the calculation of the nonequilibrium current through a single-electron transistor near the de-

generacy point. In this case, the single-electron box is connected to two separate leads, in between which a voltage bias is applied. The linear response of such a system was computed for strong tunneling by Furusaki and Matveev,⁶⁴ under the stringent assumption that each lead is coupled to different conduction-electron modes within the box (i.e., no coherent propagation between the two leads⁶⁵). This assumption, which corresponds to a four-channel Kondo Hamiltonian, has far-reaching implications for the zero-temperature conductance, which vanishes at the degeneracy point for any asymmetry in the couplings to the left and right leads.⁶⁴ In the general case we expect, though, some overlap between the modes coupled to the left and right leads, which should restore the two-channel Kondo picture for tunneling at sufficiently low temperatures. Whether this results in a square-root voltage and temperature dependence of the differential conductance as in scattering off TLS remains to be seen.

Lastly, one can exploit the KNCA to study the STM spectra around an isolated Kondo impurity placed on a d -wave superconductor. Such a setting may be realized in recent STM experiments on Zn impurities in $\text{Bi}_2\text{Sr}_2\text{CaCu}_2\text{O}_{8+\delta}$.⁶⁶ While large- N mean-field theories for the STM spectra around an isolated magnetic adatom are expected to capture the main qualitative features,^{67,68} these approaches are subject to various limitations, and are quantitatively inaccurate. The KNCA, while not free of shortcomings, should provide a more accurate framework for describing the STM spectra.

ACKNOWLEDGEMENTS

A.S. is grateful to Frithjof Anders, Daniel Cox, and Matthias Hettler, for many useful discussions. E.L. and A.S. were supported in part by the Centers of Excellence Program of the Israel science foundation, founded by The Israel Academy of Science and Humanities.

APPENDIX A: DETAILS OF THE KNCA

1. Derivation of the magnetic NCA equations

In the presence of a nonzero magnetic field, spin up and spin down are no longer equivalent. This complicates the structure of the KNCA equations, which involve in addition to the A_μ coefficients of Eqs. (22)–(23) also the following combinations:

$$\Gamma_0 = (J_0 + J_z)/4, \quad \Gamma_\perp = (J_x + J_y)/4, \quad (\text{A1})$$

$$\Lambda_0 = (J_0 - J_z)/4, \quad \Lambda_\perp = (J_x - J_y)/4. \quad (\text{A2})$$

Adopting the 4×4 matrix convention of Eqs. (17)–(18), Fig. 9 shows the building block of the NCA self-energy diagrams of Fig. 2, which we denote by

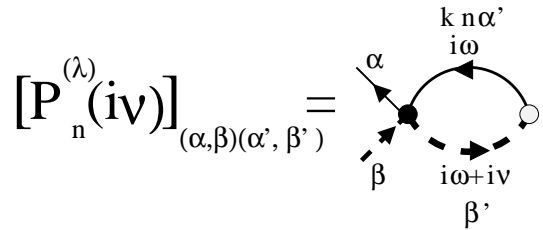


FIG. 9. Diagrammatic representation of $P_n^{(\lambda)}(i\nu)$, which serves as the building block of the NCA self-energy diagram of Fig. 2. $P_n^{(\lambda)}(i\nu)$ consists of a particle-hole bubble and a bare vertex attached at one end. Here α, β, α' , and β' are spin labels, n is a conduction-electron channel index, and there is an implicit summation over the conduction-electron momentum index k . Dashed lines represent fully dressed f Green functions.

$[P_n^{(\lambda)}(i\nu)]_{(\alpha, \beta)(\alpha', \beta')}$. It consists of a particle-hole bubble and a bare vertex attached at one end. Upon projection, $P_n(z) = \lim_{\lambda \rightarrow -\infty} P_n^{(\lambda)}(z - \lambda)$ takes the form

$$P_n(z) = \begin{bmatrix} \Gamma_0 \Pi_\uparrow(z) & 0 & 0 & \Gamma_\perp \Pi_\downarrow(z) \\ 0 & \Lambda_0 \Pi_\downarrow(z) & \Lambda_\perp \Pi_\uparrow(z) & 0 \\ 0 & \Lambda_\perp \Pi_\downarrow(z) & \Lambda_0 \Pi_\uparrow(z) & 0 \\ \Gamma_\perp \Pi_\uparrow(z) & 0 & 0 & \Gamma_0 \Pi_\downarrow(z) \end{bmatrix}, \quad (\text{A3})$$

where

$$\Pi_\sigma(z) = - \sum_k f(\epsilon_k) G_\sigma(z + \epsilon_k) \quad (\text{A4})$$

is the projected bubble. Here we have written the matrix $P_n(z)$ with respect to the basis $(\uparrow, \uparrow) \leftrightarrow 1$, $(\downarrow, \uparrow) \leftrightarrow 2$, $(\uparrow, \downarrow) \leftrightarrow 3$, and $(\downarrow, \downarrow) \leftrightarrow 4$, and made use of the fact the pseudo-fermion Green function is diagonal in the spin index. Note that P does not depend on the channel index n , which is omitted hereafter.

Using the above matrix convention, the ladder diagram of Fig. 2 is conveniently reduced to a geometric series in the matrix P . The resulting expression for the projected pseudo-fermion self-energy reads⁴⁸

$$\Sigma_\sigma(z) = -M \sum_{\alpha=\uparrow, \downarrow} \sum_k f(-\epsilon_k) \left[\frac{1}{1 - P(z - \epsilon_k)} V \right]_{(\alpha\sigma)(\alpha\sigma)}, \quad (\text{A5})$$

where M is the number of conduction-electron channels, and V is the interaction matrix of Eq. (18). The final task in deriving the KNCA equations is to invert the $1 - P$ matrix in Eq. (A5). For a zero magnetic field, when $\Pi_\uparrow(z)$ and $\Pi_\downarrow(z)$ are equal, one readily obtains Eqs. (19)–(21). For a nonzero magnetic field, when $\Pi_\uparrow(z)$ and $\Pi_\downarrow(z)$ differ, a more complicated expression is obtained. Explicitly, $\Sigma_\sigma(z)$ takes the form

$$\Sigma_\sigma(z) = \frac{M}{2} \sum_k f(-\epsilon_k) \Delta_\sigma(z - \epsilon_k), \quad (\text{A6})$$

where

$$\Delta_\sigma(z) = \frac{-2\Gamma_0 + 2(\Gamma_0^2 - \Gamma_\perp^2)\Pi_{-\sigma}(z)}{[1 - \Gamma_0\Pi_\uparrow(z)][1 - \Gamma_0\Pi_\downarrow(z)] - \Gamma_\perp^2\Pi_\uparrow(z)\Pi_\downarrow(z)} + \frac{-2\Lambda_0 + 2(\Lambda_0^2 - \Lambda_\perp^2)\Pi_{-\sigma}(z)}{[1 - \Lambda_0\Pi_\uparrow(z)][1 - \Lambda_0\Pi_\downarrow(z)] - \Lambda_\perp^2\Pi_\uparrow(z)\Pi_\downarrow(z)}. \quad (\text{A7})$$

Equations (A4), (A6), and (A7) constitute the full set of KNCA equations for a general nonzero magnetic field. For a zero magnetic field, they properly reduce to Eqs. (19)–(21).

2. Negative-frequency spectral functions

Although all relevant physical information is contained in principle in the ordinary pseudo-fermion spectral functions, numerical considerations dictate the introduction of yet another set of functions. To see this we note that the evaluation of any physical observable necessarily involves the integral of a pseudo-fermion spectral function multiplied by a Boltzmann factor that diverges for large negative energies. Hence the dominant contribution to such integrals comes from a regime where the pseudo-fermion spectral functions are exponentially small. Since it is numerically impossible to maintain such an exponential accuracy when solving the ordinary set of KNCA equations, an alternative approach is required. This is achieved by absorbing the above-mentioned Boltzmann factor into the definition of the negative-frequency spectral functions,

$$a_\sigma(\epsilon) = -\frac{1}{\pi}e^{\beta(\epsilon_0 - \epsilon)}\text{Im}\{G_\sigma(\epsilon + i\delta)\}, \quad (\text{A8})$$

and deriving an alternative set of equations directly for the functions $a_\sigma(\epsilon)$. In the above equation, $\beta = 1/k_B T$ is the inverse temperature, and ϵ_0 is an arbitrary numerical parameter, chosen to avoid exponentially large numbers.⁶⁹ The main physical quantities of interest are conveniently expressed in terms of the negative-frequency spectral functions. Specifically, the impurity contribution to the partition function, Eq. (16), is given by

$$Z_{imp} = e^{-\beta\epsilon_0} \int_{-\infty}^{\infty} [a_\uparrow(\epsilon) + a_\downarrow(\epsilon)] d\epsilon, \quad (\text{A9})$$

while the impurity magnetization is expressed as

$$M(H, T) = \frac{1}{2}\mu_B g J \frac{\int_{-\infty}^{\infty} [a_\uparrow(\epsilon) - a_\downarrow(\epsilon)] d\epsilon}{\int_{-\infty}^{\infty} [a_\uparrow(\epsilon) + a_\downarrow(\epsilon)] d\epsilon}. \quad (\text{A10})$$

To derive an alternative set of equations for the negative-frequency spectral functions, it is necessary to take the imaginary parts of Eqs. (A4), (A6) and (A7), and explicitly multiply them by the Boltzmann factor $e^{\beta(\epsilon_0 - \epsilon)}$. Upon doing so, one arrives at the following set of KNCA equations for the negative-frequency functions:

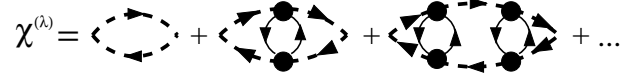


FIG. 10. NCA diagrams for the zero-field susceptibility of a Kondo impurity, as derived from the Kubo formula. Here filled circles represent dressed vertices (see Fig. 13), while dashed lines stand for fully dressed f Green functions. In the Coqblin-Schrieffer limit, all higher order terms vanish and only the bare bubble is left. In contrast, all terms contribute to the susceptibility of a generic Kondo Hamiltonian.

$$a_\sigma(\epsilon) = \frac{M}{2}|G_\sigma(\epsilon)|^2 \sum_k f(\epsilon_k) d_\sigma(\epsilon - \epsilon_k) \quad (\text{A11})$$

with

$$d_\sigma(\epsilon) = \varphi_\sigma(\epsilon) \sum_k f(-\epsilon_k) a_\sigma(\epsilon + \epsilon_k) + \psi_\sigma(\epsilon) \sum_k f(-\epsilon_k) a_{-\sigma}(\epsilon + \epsilon_k). \quad (\text{A12})$$

Here $\varphi_\sigma(\epsilon)$ and $\psi_\sigma(\epsilon)$ are two rather complicated expressions given by

$$\varphi_\sigma(\epsilon) = \frac{2C^2(\Gamma_0, \Gamma_\perp, \Pi_{-\sigma})}{|(1 - \Gamma_0\Pi_\uparrow)(1 - \Gamma_0\Pi_\downarrow) - \Gamma_\perp^2\Pi_\uparrow\Pi_\downarrow|^2} \quad (\text{A13})$$

+ (the same with Γ_0, Γ_\perp and Λ_0, Λ_\perp interchanged)

and

$$\psi_\sigma(\epsilon) = \frac{2C(\Gamma_0, \Gamma_\perp, \Pi_{-\sigma})C(\Gamma_0, \Gamma_\perp, \Pi_\sigma)}{|(1 - \Gamma_0\Pi_\uparrow)(1 - \Gamma_0\Pi_\downarrow) - \Gamma_\perp^2\Pi_\uparrow\Pi_\downarrow|^2} + 2(\Gamma_0^2 - \Gamma_\perp^2)\text{Re}\left\{\frac{1}{(1 - \Gamma_0\Pi_\uparrow)(1 - \Gamma_0\Pi_\downarrow) - \Gamma_\perp^2\Pi_\uparrow\Pi_\downarrow}\right\}$$

+ (the same with Γ_0, Γ_\perp and Λ_0, Λ_\perp interchanged),

where

$$C(x, y, z) = x + (y^2 - x^2)\text{Re}\{z\}. \quad (\text{A15})$$

In Eqs. (A13)–(A14), we have omitted for conciseness the arguments of $\Pi_\uparrow(\epsilon + i\delta)$ and $\Pi_\downarrow(\epsilon + i\delta)$.

Note that the negative-frequency equations explicitly depend on $G_\sigma(z)$ and $\Pi_\sigma(z)$, hence the negative-frequency and ordinary KNCA equations must be solved simultaneously. This is done by repeated numerical iterations until convergence is reached. As is always the case with numerical solutions of NCA-type equations, the key to high-precision numerics is in a well-designed grid of mesh points that scatter mesh points more densely near the threshold and peaks of the relevant functions. To this end, we have used a combination of linear and logarithmic grids. As a critical test for the precision of our numerical code, we have checked in all our runs that the pseudo-fermion spectral functions fulfilled the spectral sum rule to within one part in one thousand (i.e., 0.1%).

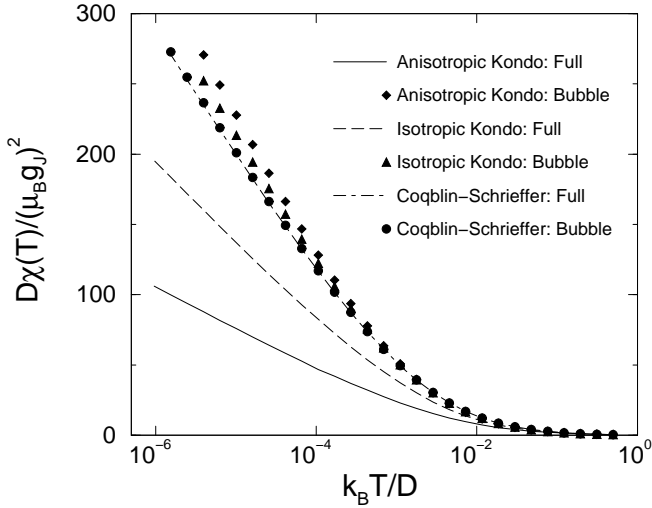


FIG. 11. Comparison between the simple magnetization bubble and the full zero-field susceptibility, obtained by differentiating $M(H, T)$ with respect to H . All curves refer to the two-channel case, with $\rho_0 A_0$ held fixed at 0.2. While the two procedures give identical results in the Coqblin-Schrieffer limit (we use $\rho_0 J_0 = \rho_0 J = 0.2$), substantial deviations are found for the isotropic and anisotropic Kondo models (we use $\rho_0 J = 0.2667$ for the isotropic Kondo model, and $J_z = 0$ and $\rho_0 J_\perp = 0.4$ for the anisotropic Kondo Model). In the latter two cases, the effect of the magnetic vertex correction is to significantly reduce the slope of the log- T diverging term in $\chi(T)$.

3. Magnetic vertex correction

As mentioned in the main text, we have calculated the magnetic susceptibility $\chi(H, T)$ by numerically differentiating the magnetization of Eq. (A10) with respect to H . An interesting observation has to do with the calculation of the zero-field susceptibility, $\chi(T)$. For the Anderson and Coqblin-Schrieffer models, one traditionally computes the zero-field susceptibility from the Kubo formula, which reduces in the NCA to a simple bubble diagram.³⁴ For a Kondo model, however, there is a nontrivial magnetic vertex correction that cannot be neglected. Fig. 10 depicts the NCA susceptibility diagrams for a generic Kondo model. In addition to the simple bubble, there is a magnetic vertex correction in the form of a ladder diagram. Each rung of the ladder consists of two dressed vertices (displayed in Fig. 13), connected by a conduction-electron bubble. Since the rungs are frequency dependent, a direct evaluation of the entire series requires the solution of an integral equation, which is far more complicated than numerical differentiation of the magnetization curve.

While in the Coqblin-Schrieffer limit, $J_0 = J_x = J_y = J_z$, it is possible to show that only the simple bubble survives,⁷⁰ for a generic Kondo model there are non-negligible contributions coming from the magnetic ver-

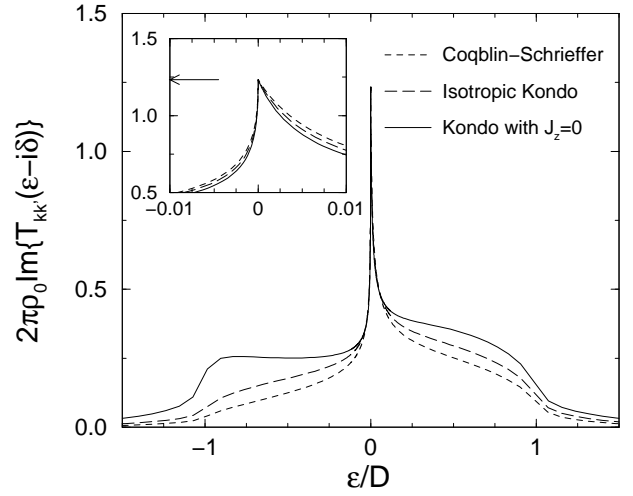


FIG. 12. Imaginary part of the conduction-electron T -matrix, as obtained from the KNCA. Here, the solid line corresponds to the anisotropic two-channel Kondo model with $J_z = 0$ and $\rho_0 J_\perp = 0.4$ ($k_B T_K/D = 3.85 \times 10^{-3}$); the long-dashed line is for the isotropic two-channel Kondo model with $\rho_0 J = 0.2667$ ($k_B T_K/D = 2 \times 10^{-3}$); and the short-dashed line is for the two-channel Coqblin-Schrieffer model with $\rho_0 J_0 = \rho_0 J = 0.2$ ($k_B T_K/D = 1.35 \times 10^{-3}$). The temperature in all curves is equal to $T/T_K = 0.01$. In accordance with the analytic treatment of the NCA equations at zero temperature,³⁵ the T -matrix has a cusp at zero energy, with a strong particle-hole asymmetry. All curves fall within 1.5% from the predicted zero-temperature NCA value of $2\pi\rho_0 \text{Im}\{T_{kk'}(0 - i\delta)\} = \pi^2/8$ (marked by an arrow in the inset).

tex correction. For the two-channel case, this is demonstrated in Fig. 11, where the results of the bare bubble are compared with the full zero-field susceptibility obtained by differentiating $M(H, T)$. As required, the two procedures are indistinguishable in the Coqblin-Schrieffer limit, establishing the numerical accuracy of our differentiation routine. A different picture is recovered, however, for the isotropic and anisotropic Kondo models. In both cases the slope of the log- T diverging term in $\chi(T)$ is significantly reduced upon going from the simple bubble diagram to the full susceptibility. This effect is particularly pronounced for the anisotropic Hamiltonian of Eq. (9), where nearly a three-fold reduction is found in the slope of the log- T component of $\chi(T)$. Thus, the magnetic vertex correction contains essential contributions to the low-temperature susceptibility of the two-channel Kondo model.

4. Conduction-electron T -matrix

Another quantity of interest in the theory of dilute magnetic alloys is the conduction-electron T -matrix, defined by the expansion

$$G_{kk',\sigma}(z) = G_{k\sigma}^{(0)}(z)\delta_{k,k'} + G_{k\sigma}^{(0)}(z)T_{kk',\sigma}(z)G_{k'\sigma}^{(0)}(z). \quad (\text{A16})$$

Here $G_{kk',\sigma}(z)$ is the Fourier representation of the dressed conduction-electron Green function

$$G_{kk',\sigma}(\tau) = -\langle T_{\tau} c_{kn\sigma}(\tau) c_{k'n\sigma}^{\dagger}(0) \rangle, \quad (\text{A17})$$

and $G_{k\sigma}^{(0)}(z) = 1/(z - \epsilon_k)$ is the bare conduction-electron Green function. For a nondegenerate Anderson impurity, $T_{kk',\sigma}(z)$ is equal to $V^2 G_{imp,\sigma}(z)$, where V is the hybridization matrix element (assumed here to be k independent), and $G_{imp,\sigma}(z)$ is the dressed impurity Green function. Hence the calculation of the T -matrix is reduced to that of the dressed impurity Green function. For a Kondo impurity there is no analogous relation, and $T_{kk',\sigma}(z)$ needs to be constructed directly from Eq. (A16).

Within the slave-fermion representation, the T -matrix is related to the *unprojected* conduction-electron self-energy through

$$T_{kk',\sigma}(z) = \frac{1}{Z_{imp}} \lim_{\lambda \rightarrow -\infty} e^{-\beta\lambda} \Sigma_{kk',\sigma}^{(\lambda)}(z). \quad (\text{A18})$$

Using the NCA class of diagrams for the conduction-electron self-energy, and in the absence of an applied magnetic field, one obtains

$$T_{kk'}(z) = \frac{e^{-\beta\epsilon_0}}{2Z_{imp}} \int_{-\infty}^{\infty} [d(\epsilon)G(z + \epsilon) - a(\epsilon)\Delta(\epsilon - z)] d\epsilon, \quad (\text{A19})$$

where $G(z)$ is the pseudo-fermion Green function, $a(\epsilon)$ is the negative-frequency spectral function of Eq (A8), $\Delta(z)$ is defined in Eq. (20), and $d(\epsilon)$ is given by Eq. (A12). Note that all spin indices have been dropped in Eq. (A19) due to the equivalence of the two spin orientations for a zero magnetic field. Also notice that $T_{kk'}(z)$ has no explicit dependence on k and k' , as is characteristic of purely local scattering.

Figure 12 shows the imaginary part of the KNCA conduction-electron T -matrix, for each of the Coqblin-Schrieffer, isotropic Kondo, and anisotropic Kondo models. The coupling constants were adjusted in each model as to give $\rho_0 A_0 = 0.2$, while the temperature $T/T_K = 0.01$ is sufficiently low in order for fully developed Kondo peaks to be seen. Two points are noteworthy. First, there is a clear asymmetry in the energy dependence of $\text{Im}\{T_{kk'}(\epsilon + i\delta)\}$, which for the isotropic and anisotropic Kondo models is in violation of the underlying particle-hole symmetry. This asymmetry persists from high energies, $|\epsilon| \sim D$, down to at low energies, $|\epsilon| \lesssim T_K$. As discussed in Appendix B, it stems from the omission of particle-particle bubbles within the NCA. Thus, the asymmetric line shape of the Kondo resonance is an inherent feature of the NCA class of diagrams, and is not due to the lack of an underlying particle-hole symmetry, as previously asserted for the multi-channel Anderson model.³⁵

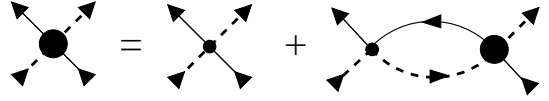


FIG. 13. Renormalization of the bare interaction within the KNCA. In the diagrams of Fig 2, the bare vertex is dressed by a ladder of particle-hole bubbles, each composed of one (bare) conduction-electron line and one (fully dressed) pseudo-fermion line.

The second point to notice is that all curves approach the predicted zero-temperature NCA value of $2\pi\rho_0\text{Im}\{T_{kk'}(0 - i\delta)\} = \pi^2/8$.³⁵ Since this value is determined by the NCA threshold exponents, which are unchanged in going from the two-channel Anderson to the isotropic and anisotropic Kondo models, then the same zero-temperature value applies to all models.

APPENDIX B: COMPARISON WITH POOR-MAN'S SCALING

Considerable insight into the origin of the NCA setbacks can be gained by comparing the KNCA with Anderson's poor-man's scaling.⁷¹ Specifically, the KNCA set of diagrams can be viewed as a ladder renormalization of the bare interaction, as illustrated in Fig. 13. The basic renormalization of the bare vertex is due to particle-hole bubbles. This should be contrasted with poor-man's scaling, where two distinct types of renormalizations are found: particle-hole and particle-particle bubbles (see Fig. 14). Thus, it appears that the KNCA corresponds to retaining only the particle-hole processes within poor-man's scaling (although additional higher-order terms do enter the KNCA through the self-consistent dressing of the pseudo-fermion Green functions).

To substantiate this correspondence between the KNCA and poor-man's scaling, we have rewritten the well-known renormalization-group (RG) equations for the dimensionless coupling constants $\tilde{J}_\mu = \rho_0 J_\mu$ ($\mu = 0, x, y, z$), by separating the contributions of the two diagrams of Fig. 14. Labeling the contributions of the particle-hole and particle-particle diagrams by *ph* and *pp*, respectively, the corresponding equations read

$$\left. \frac{d\tilde{J}_i}{dl} \right|_{ph} = \frac{1}{2} [\tilde{J}_j \tilde{J}_k + \tilde{J}_0 \tilde{J}_i], \quad (\text{B1})$$

$$\left. \frac{d\tilde{J}_0}{dl} \right|_{ph} = \frac{1}{4} \sum_{\mu=0,x,y,z} \tilde{J}_\mu^2, \quad (\text{B2})$$

and

$$\left. \frac{d\tilde{J}_i}{dl} \right|_{pp} = \frac{1}{2} [\tilde{J}_j \tilde{J}_k - \tilde{J}_0 \tilde{J}_i], \quad (\text{B3})$$

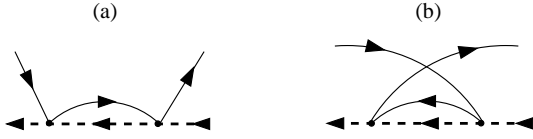


FIG. 14. Renormalization of the interaction within poor-man's scaling. We distinguish between (a) processes involving the excitation of a high-energy electron (particle-hole bubble) and (b) processes involving the excitation of a high-energy hole (particle-particle bubble). The KNCA retains only the particle-hole bubble of (a), albeit with self-consistent dressing of the pseudo-fermion Green functions.

$$\left. \frac{d\tilde{J}_0}{dl} \right|_{pp} = -\frac{1}{4} \sum_{\mu=0,x,y,z} \tilde{J}_\mu^2, \quad (\text{B4})$$

where l is equal to $\ln(D_0/D)$, and i, j , and k represent a cyclic permutation of x, y , and z . Here D is the running bandwidth, and D_0 is the bare bandwidth. By combining the two sets of equations listed above, one recovers the standard RG equations:⁷¹

$$\frac{d\tilde{J}_i}{dl} = \tilde{J}_j \tilde{J}_k, \quad (\text{B5})$$

$$\frac{d\tilde{J}_0}{dl} = 0. \quad (\text{B6})$$

If we artificially ignore the particle-particle contributions of Eqs. (B3)–(B4) and settle with Eqs. (B1)–(B2) for $d\tilde{J}_\mu/dl$, it is easy to verify that

$$\tilde{A}_0 = \frac{1}{4} (\tilde{J}_0 + \tilde{J}_x + \tilde{J}_y + \tilde{J}_z), \quad (\text{B7})$$

$$\tilde{A}_i = \frac{1}{4} (\tilde{J}_0 + 2\tilde{J}_i - \tilde{J}_x - \tilde{J}_y - \tilde{J}_z) \quad (\text{B8})$$

($i = x, y, z$) obey the single differential equation

$$\left. \frac{d\tilde{A}_\mu}{dl} \right|_{ph} = \tilde{A}_\mu^2. \quad (\text{B9})$$

Equation (B9) has the exact same form as the standard RG equation for the dimensionless exchange coupling in the isotropic Kondo model.⁷¹ As is well known, its outcome depends on the sign of the bare coupling constant. If \tilde{A}_μ is initially positive (“antiferromagnetic” coupling) then this coupling flows towards strong coupling; otherwise (“ferromagnetic” coupling) it flows to weak coupling. In the former case, a nonperturbative energy scale $T_\mu \sim D_0 \exp[-1/\rho_0 A_\mu]$ emerges, below which \tilde{A}_μ of Eq. (B9) becomes of order unity. If several \tilde{A}_μ simultaneously flow towards strong coupling, then the largest of the T_μ 's will emerge as the actual low-energy scale.

From this analysis it is clear that Eqs. (B1)–(B2) flow towards strong coupling whenever at least one of the A_μ 's

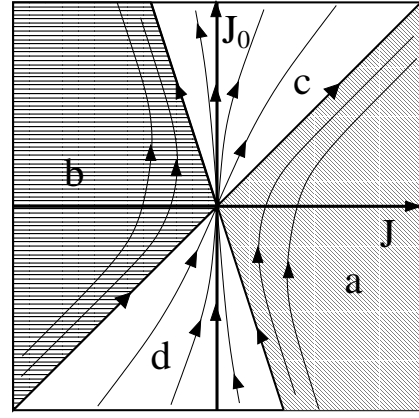


FIG. 15. RG flow trajectories corresponding to Eqs. (B1)–(B2) with an isotropic spin-exchange coupling J . There are four different RG regimes: (a) $-3J < J_0 \leq J$, where only \tilde{A}_0 is relevant; (b) $J < J_0 \leq -3J$, where only \tilde{A}_0 is irrelevant; (c) $-3J, J < J_0$, where all the \tilde{A}_μ 's are relevant; and (d) $J_0 \leq -3J, J$, where all the \tilde{A}_μ 's are irrelevant. The flow in region (a) and in the $J > 0$ part of region (c) is towards $J_0, J = \infty$ and $J_0/J = 1$; in region (b) and in the $J < 0$ part of region (c) the flow is towards $J_0, -J = \infty$ and $J_0/J = -3$; the flow along the $J = 0$ line in region (c) is towards $J_0 = \infty$ and $J = 0$; and in region (d) the flow is towards $J_0 = J = 0$.

of Eqs. (22)–(23) is positive. The underlying nonperturbative energy scale that emerges then is given by

$$T_K^{(ph)} \sim D_0 \exp\left(-\frac{1}{\rho_0 A_{\max}}\right), \quad (\text{B10})$$

where A_{\max} is the largest of the positive A_μ 's. Note that for antiferromagnetic couplings with $J_\perp > 0$, A_{\max} is always given by A_0 .

An identical picture is recovered within the KNCA equations for a zero magnetic field, Eqs. (19)–(21). Here the flow towards strong coupling is manifest in the divergence of $\Delta(\epsilon + i\delta)$ at the threshold energy as $T \rightarrow 0$,⁷² which happens whenever at least one of the A_μ 's is positive. If more than one A_μ coefficient is positive then only that $A_\mu/[1 - A_\mu \Pi(\epsilon + i\delta)]$ component of $\Delta(\epsilon + i\delta)$ corresponding to A_{\max} diverges, while all other components remain finite.⁷³ The nonperturbative energy scale underlying the NCA is then precisely given by Eq. (B10), establishing the intimate connection between the KNCA and the restricted version of poor-man's scaling where only particle-hole processes are retained. (Obviously, the two approaches are not entirely equivalent, as the KNCA also includes self-consistent dressing of the pseudo-fermion Green functions.)

We can now exploit this basic relation between the KNCA and Eqs. (B1)–(B2) to clarify the setbacks of the KNCA. For simplicity, let us focus on the isotropic case, $J_x = J_y = J_z = J$. From Eq. (B2) one readily sees that, starting from $J_0 = 0$, a nonzero potential scattering is immediately generated. This is to be contrasted with the full set of RG equations, in which

potential scattering is exactly marginal. Thus, starting from a particle-hole symmetric Hamiltonian, the omission of the particle-hole symmetry contributions necessarily breaks particle-hole symmetry, leading, for example, to the asymmetric energy dependence of the conduction-electron T -matrix within the KNCA (see Fig 12).

More significantly, the interplay between the spin-exchange couplings and the ever-increasing potential scattering substantially alters the RG flow diagram. In Fig. 15, the RG flow trajectories corresponding to Eqs. (B1)–(B2) are plotted in the $J - J_0$ plane. While the full set of RG equations, Eqs. (B5)–(B6), support only horizontal trajectories, none of the trajectories of Eqs. (B1)–(B2) are horizontal. Overall there are four different regimes: (a) $-3J < J_0 \leq J$, where only \tilde{A}_0 is relevant; (b) $J < J_0 \leq -3J$, where only \tilde{A}_0 is irrelevant; (c) $-3J, J < J_0$, where all the \tilde{A}_μ 's are relevant; and (d) $J_0 \leq -3J, J$, where all the \tilde{A}_μ 's are irrelevant. Thus, with the exception of region (d), Eqs. (B1)–(B2) flow towards some kind of strong coupling, including in the case of ferromagnetic coupling. The emergence of a ferromagnetic Kondo-type effect within the KNCA is therefore an artifact of the omission of particle-particle diagrams.

Finally, if one naively extends Eqs. (B1)–(B2) to the strong-coupling regime, then four different fixed points are recovered: (i) $J_0, J = \infty$ and $J_0/J = 1$ [approached from region (a) and from the $J > 0$ part of region (c)]; (ii) $J_0, -J = \infty$ and $J_0/J = -3$ [approached from region (b) and from the $J < 0$ part of region (c)]; (iii) $J_0 = \infty$ and $J = 0$ [approached from the $J = 0$ line in region (c)]; and (iv) $J_0 = J = 0$ [approached from region (d)]. Interestingly, from the solution of the KNCA equations at $T = 0$ one also finds four different low-temperature behaviors, corresponding to the precise four basins of attraction listed above.

APPENDIX C: BEYOND THE NCA

From the discussion in the preceding Appendix it is clear that any proper theory of the Kondo effect must include particle-particle and particle-hole processes on equal footing. Diagrammatically, this necessitates going beyond the NCA class of diagrams, which is the objective of the present Appendix.

Figure 16 displays a formally exact representation of the pseudo-fermion self-energy. The first line in Fig. 16 represents all pseudo-fermion self-energy diagrams. The full circle marks the full vertex function, by which we mean the collection of all connected four-legged diagrams with one incoming and one outgoing pseudo-fermion line, and one incoming and one outgoing conduction-electron line. We classify the vertex diagrams according to two classes. The particle-hole irreducible (PHI) vertex function is defined as the sum of all vertex diagrams that cannot be disconnected into two distinct vertex diagrams by cutting one internal conduction-electron line and one

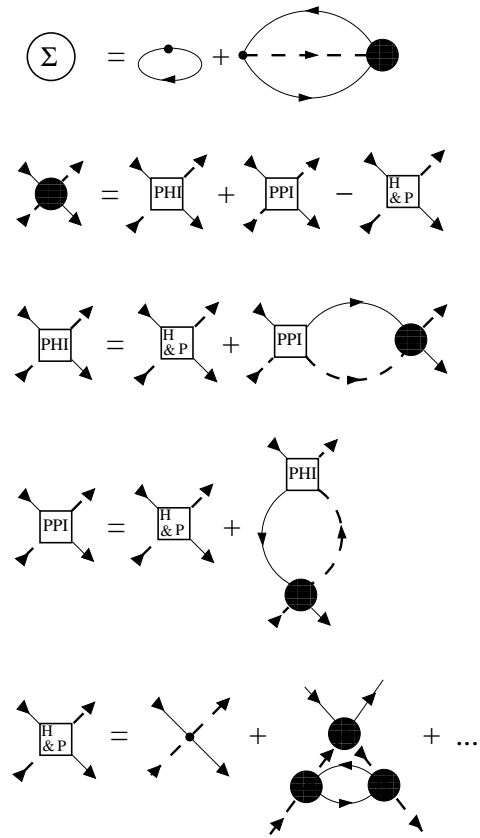


FIG. 16. A formally exact representation of the pseudo-fermion self-energy in terms of irreducible vertex functions. The first line represents all pseudo-fermion self-energy diagrams. The full circle marks the full vertex function, i.e., the collection of all connected four-legged diagrams with one incoming and one outgoing pseudo-fermion line, and one incoming and one outgoing conduction-electron line. The full vertex function is expressed in turn in the second line via the more elementary particle-hole irreducible (PHI), particle-particle irreducible (PPI), and both particle-hole and particle-particle irreducible (PHI&PPI) vertices. For precise definitions, see text.

internal pseudo-fermion line propagating in *opposite* directions (third line of Fig. 16). The particle-particle irreducible (PPI) vertex function is defined by a similar collection of diagrams, that cannot be disconnected into two distinct vertex diagrams by cutting one internal conduction-electron line and one internal pseudo-fermion line propagating in the *same* direction (fourth line of Fig. 16). Note that each vertex diagram is a member of at least one of the two classes PHI and PPI. Some vertex diagrams, like the bare vertex, are both PHI and PPI. We refer hereafter to these joint diagrams as PHI&PPI. Hence the full vertex function is equal to the sum of the PHI and PPI vertex functions, minus the PHI&PPI diagrams which are counted twice.

There are infinitely many diagrams that are PHI&PPI, the first two of which are depicted on the fifth line of

Fig. 16. Provided one is able to sum the entire class of PHI&PPI diagrams, then Fig. 16 constitutes an exact representation of the pseudo-fermion self-energy, as well as of the PHI, PPI, and full vertex functions. In practice, it is impossible to sum all the PHI&PPI diagrams. However, any selection of a subclass of PHI&PPI diagrams that preserves particle-hole symmetry defines an approximation scheme that necessarily respects particle-hole symmetry. The simplest choice for the PHI&PPI vertex function is to settle with the bare vertex, which defines the parquet class of diagrams. Below we focus on this particular choice.

Each of the PHI, PPI and full vertex functions depend on three energy variables, as well as on the spin indices of the four external legs. Adopting the notation of Eq. (17), we label the spin index of the outgoing (incoming) conduction-electron line by α (α'), and that of the outgoing (incoming) pseudo-fermion line by β' (β). As for the energy variables, we choose to work with the following combinations: (i) The particle-hole energy, z_h , corresponding to the outgoing pseudo-fermion frequency minus the incoming conduction-electron frequency; (ii) The particle-particle energy, z_p , corresponding to the incoming pseudo-fermion frequency plus the incoming conduction-electron frequency; and (iii) The pseudo-fermion energy, z_f , corresponding to the outgoing pseudo-fermion frequency. For each of the PHI, PPI, and full vertex functions, the projected functions are defined as

$$\Gamma_{\alpha\beta;\alpha'\beta'}(z_h, z_p, z_f) = \lim_{\lambda \rightarrow -\infty} \Gamma_{\alpha\beta;\alpha'\beta'}^{(\lambda)}(z_h - \lambda, z_p - \lambda, z_f - \lambda), \quad (\text{C1})$$

where $\Gamma_{\alpha\beta;\alpha'\beta'}^{(\lambda)}$ is the corresponding unprojected function.

Approximating the PHI&PPI vertex function by the bare vertex, one can show that the projected PHI, PPI, and full vertex functions have the form

$$\Gamma_{\alpha\beta;\alpha'\beta'}^{(PHI)}(z_h, z_p, z_f) = \frac{1}{4} \sum_{\mu=0,x,y,z} \mathcal{H}_\mu(z_h, z_p, z_f) \sigma_{\alpha\alpha'}^\mu \sigma_{\beta'\beta}^\mu, \quad (\text{C2})$$

$$\Gamma_{\alpha\beta;\alpha'\beta'}^{(PPI)}(z_h, z_p, z_f) = \frac{1}{4} \sum_{\mu=0,x,y,z} \mathcal{P}_\mu(z_h, z_p, z_f) \sigma_{\alpha\alpha'}^\mu \sigma_{\beta'\beta}^\mu, \quad (\text{C3})$$

$$\Gamma_{\alpha\beta;\alpha'\beta'}^{(Full)}(z_h, z_p, z_f) = \frac{1}{4} \sum_{\mu=0,x,y,z} \mathcal{J}_\mu(z_h, z_p, z_f) \sigma_{\alpha\alpha'}^\mu \sigma_{\beta'\beta}^\mu. \quad (\text{C4})$$

Thus, each of the above vertex functions retains the form of the bare interaction, only with renormalized couplings that are energy dependent. Furthermore, one has the identity $\mathcal{J}_\mu = \mathcal{H}_\mu + \mathcal{P}_\mu - J_\mu$, where J_μ are the bare coupling constants. The PHI and PPI vertex functions are given in turn by the following set of coupled integral equations:

$$\mathcal{P}_0(z_h, z_p, z_f) = J_0 - \sum_{\mu=0,x,y,z} [\mathcal{H}_\mu \oplus \mathcal{J}_\mu], \quad (\text{C5})$$

$$\begin{aligned} \mathcal{P}_i(z_h, z_p, z_f) &= J_i - [\mathcal{H}_0 \oplus \mathcal{J}_i] - [\mathcal{H}_i \oplus \mathcal{J}_0] \\ &\quad - \sum_{j,m=x,y,z} \epsilon_{ijm}^2 [\mathcal{H}_j \oplus \mathcal{J}_m], \end{aligned} \quad (\text{C6})$$

$$\mathcal{H}_0(z_h, z_p, z_f) = J_0 + \sum_{\mu=0,x,y,z} [\mathcal{P}_\mu \ominus \mathcal{J}_\mu], \quad (\text{C7})$$

$$\begin{aligned} \mathcal{H}_i(z_h, z_p, z_f) &= J_i + [\mathcal{P}_0 \ominus \mathcal{J}_i] + [\mathcal{P}_i \ominus \mathcal{J}_0] \\ &\quad - \sum_{j,m=x,y,z} \epsilon_{ijm}^2 [\mathcal{P}_j \ominus \mathcal{J}_m], \end{aligned} \quad (\text{C8})$$

where ϵ_{ijm} is the antisymmetric tensor, i is equal to x, y , or z , and the convolution operators \oplus and \ominus stand for

$$\begin{aligned} [\mathcal{H}_\mu \oplus \mathcal{J}_\nu] &= \frac{1}{4} \sum_k f(\epsilon_k) G(z_h + \epsilon_k) \mathcal{H}_\mu(z_h, z_p + \Delta_1, z_f) \\ &\quad \times \mathcal{J}_\nu(z_h, z_p + \Delta_2, z_f + \Delta_2), \end{aligned} \quad (\text{C9})$$

$$\begin{aligned} [\mathcal{P}_\mu \ominus \mathcal{J}_\nu] &= \frac{1}{4} \sum_k f(-\epsilon_k) G(z_p - \epsilon_k) \mathcal{J}_\nu(z_h - \Delta_2, z_p, z_f) \\ &\quad \times \mathcal{P}_\mu(z_h - \Delta_1, z_p, z_f - \Delta_1). \end{aligned} \quad (\text{C10})$$

Here Δ_1 and Δ_2 are shorthands for

$$\Delta_1 = \epsilon_k + z_f - z_p, \quad (\text{C11})$$

$$\Delta_2 = \epsilon_k + z_h - z_f. \quad (\text{C12})$$

(Note that the frequencies $z_p - z_f$ and $z_f - z_h$ are just the outgoing and incoming conduction-electron frequencies, respectively.) Omitting the constant term $(MJ_0N_e)/4$ (N_e being the total number of conduction electrons), the pseudo-fermion self-energy is equal to

$$\begin{aligned} \Sigma(z) &= \frac{M}{8} \sum_{k,k'} f(\epsilon_k) f(-\epsilon_{k'}) G(z + \epsilon_k - \epsilon_{k'}) \times \\ &\quad \sum_{\mu=0,x,y,z} J_\mu \mathcal{J}_\mu(z - \epsilon_{k'}, z + \epsilon_k, z). \end{aligned} \quad (\text{C13})$$

Equations (C5)–(C13) represent a complete summation of the parquet class of diagrams, which includes in particular all diagrams contained within poor-man's scaling. While we believe these equations are intimately related to the conserving T -matrix approach of Kroha *et al.*⁶³ for the multi-channel Anderson model, we are unable to formally link the two approaches. We further emphasize that Eqs. (C5)–(C13) apply to a general anisotropic Kondo model, ferromagnetic or antiferromagnetic, and hence extend beyond the Schrieffer-Wolff limit of the Anderson Hamiltonian.

A full self-consistent solution of Eqs. (C5)–(C13) is a difficult task, due to the three energy variables entering the coupled integral equations for $\mathcal{P}_\mu(z_h, z_p, z_f)$ and $\mathcal{H}_\mu(z_h, z_p, z_f)$. Below we resort to a crude approximate treatment, aimed at demonstrating the amendment of the KNCA flaws.

Since the onset the Kondo effect is manifest in the development of strong scattering at the Fermi level, we set the energies and thus frequencies of the incoming and outgoing conduction electrons equal to zero. [We emphasize that, upon implementing the projection of Eqs. (C1), the conduction-electron frequencies acquire the value of the bare conduction-electron energies.] We begin by noting that the energies Δ_1 and Δ_2 in each of Eqs. (C9) and (C10) correspond to the single-particle energy difference between the conduction electrons incoming and outgoing one of the vertex function in that equation — \mathcal{J}_ν for Δ_1 , and \mathcal{H}_μ or \mathcal{P}_μ for Δ_2 . Thus, since scattering in the Kondo problem is strong near the Fermi level, one expects the main contribution to the k summations in Eqs. (C9)–(C10) to come from that range in k where Δ_1 and Δ_2 are small. As a first approximation, we therefore decouple the sums in Eqs. (C9)–(C10) by setting $\Delta_1 = \Delta_2 = 0$.

The second approximation we adopt is to linearize Eqs. (C9)–(C10) by replacing the PHI and PPI vertex functions, \mathcal{H}_μ and \mathcal{P}_μ , with the bare vertex, J_μ . This clearly is a crude approximation, motivated primarily by technical considerations. It encompasses, however, the ladder summation of the KNCA. Using the above two approximations in combination with the identity $\mathcal{J}_\mu = \mathcal{P}_\mu + \mathcal{H}_\mu - J_\mu$, we arrive at the following set of equations for the full vertex functions $\mathcal{J}_\mu \equiv \mathcal{J}_\mu(z_f, z_f, z_f)$:

$$\mathcal{J}_0 = J_0 + \frac{1}{4} [\Pi_+(z_f) - \Pi_-(z_f)] \sum_{\mu=0,x,y,z} J_\mu \mathcal{J}_\mu, \quad (\text{C14})$$

$$\begin{aligned} \mathcal{J}_i &= J_i + \frac{1}{4} [\Pi_+(z_f) - \Pi_-(z_f)] [J_0 \mathcal{J}_i + J_i \mathcal{J}_0] \\ &+ \frac{1}{4} [\Pi_+(z_f) + \Pi_-(z_f)] \sum_{j,m=x,y,z} \varepsilon_{ijm}^2 J_j \mathcal{J}_m. \end{aligned} \quad (\text{C15})$$

Here, as before, i is equal to x, y , or z , while $\Pi_\pm(z)$ are the projected particle-hole and particle-particle bubbles:

$$\Pi_\pm(z) = - \sum_k f(\pm \epsilon_k) G(z \pm \epsilon_k). \quad (\text{C16})$$

Similar to the KNCA, one can estimate the exponential dependence of the Kondo temperature on $1/J_\mu$ by substituting the bare pseudo-fermion Green function into Eq. (C16), and examining the location of the zero-temperature poles in the full vertex functions $\mathcal{J}_\mu(z_f, z_f, z_f)$. For a particle-hole symmetric band, when $\Pi_+(z)$ and $\Pi_-(z)$ coincide, $\mathcal{J}_0(z_f, z_f, z_f)$ is simply equal to J_0 . Thus, there is no renormalization of the potential scattering at the Fermi level, in accordance with poor-man's scaling. In the isotropic case, $J_x = J_y = J_z = J$, the remaining components of the full vertex function are also isotropic, and are given by

$$\mathcal{J}(z_f, z_f, z_f) = \frac{J}{1 - \Pi(z_f)}. \quad (\text{C17})$$

Setting $T = 0$ and $z_f = \epsilon + i\delta$, one sees that there are no divergences in $\mathcal{J}(z_f, z_f, z_f)$ for $J < 0$, implying

the absence of a ferromagnetic Kondo effect. By contrast, $\mathcal{J}(z_f, z_f, z_f)$ diverges for $J > 0$ and $T = 0$ at $\epsilon \sim -D \exp[-1/\rho_0 J]$, which we identify with $-k_B T_K$. Hence the correct exponential dependence of T_K on $1/J$ is properly recovered. For the anisotropic Hamiltonian of Eq. (9), a similar analysis gives $k_B T_K \sim D \exp[-\sqrt{2}/\rho_0 J]$, which still deviates from the desired form of $T_K \sim D \exp[-\pi/2\rho_0 J_\perp]$, but marks a significant improvement over the KNCA.

Although the above treatment is too crude to convincingly establish the amendment of the NCA flaws, we take it as an encouraging indication for the elimination of the spurious ferromagnetic Kondo effect and the correction of the exponential dependence of T_K on $1/J_\mu$ within the proposed scheme.

-
- ¹ D. Goldhaber-Gordon, H. Shtrikman, D. Mahalu, D. Abusch-Magder, U. Meirav, and M. A. Kastner, *Nature* **391**, 156 (1998); D. Goldhaber-Gordon, J. Göres, M. A. Kastner, H. Shtrikman, D. Mahalu, and U. Meirav, *Phys. Rev. Lett.* **81**, 5225 (1998).
 - ² S. M. Cronenwett, T. H. Oosterkamp, and L. P. Kouwenhoven, *Science* **281**, 540 (1998).
 - ³ J. Schmid, J. Weis, K. Eberl, and K. von Klitzing, *Physica B* **258**, 182 (1998).
 - ⁴ F. Simmel, R. H. Blick, J. P. Kotthaus, W. Wegscheider, and M. Bichler, *Phys. Rev. Lett.* **83**, 804 (1999).
 - ⁵ W. G. van der Wiel, S. De Franceschi, T. Fujisawa, J. M. Elzerman, S. Tarucha, and L. P. Kouwenhoven, *Science* **289**, 2105 (2000).
 - ⁶ J. Li, W.-D. Schneider, R. Berndt, and B. Delley, *Phys. Rev. Lett.* **80**, 2893 (1998).
 - ⁷ V. Madhavan, W. Chen, T. Jamneala, M. F. Crommie, and N. S. Wingreen, *Science* **280**, 567 (1998).
 - ⁸ H. C. Manoharan, C. P. Lutz, and D. M. Eigler, *Nature* **403** 512 (2000).
 - ⁹ W. Chen, T. Jamneala, V. Madhavan, and M. F. Crommie, *Phys. Rev. B* **60**, 8529 (1999).
 - ¹⁰ A. Georges and Y. Meir, *Phys. Rev. Lett.* **82**, 3508 (1999).
 - ¹¹ P. Nozières and A. Blandin, *J. Physique* **41**, 193 (1980).
 - ¹² A. Zawadowski, *Phys. Rev. Lett.* **45**, 211 (1980).
 - ¹³ For a comprehensive review, see D. L. Cox and A. Zawadowski, *Adv. Phys.* **47**, 599 (1998).
 - ¹⁴ D. C. Ralph and R. A. Buhrman, *Phys. Rev. Lett.* **69**, 2118 (1992).
 - ¹⁵ D. C. Ralph, A. W. W. Ludwig, J. von Delft and R. A. Buhrman, *Phys. Rev. Lett.* **72**, 1064 (1994).
 - ¹⁶ For a recent review, see J. von Delft, D. C. Ralph, R. A. Buhrman, S. K. Upadhyay, R. N. Louie, A. W. W. Ludwig, and V. Ambegaokar, *Ann. Phys.* **263**, 1 (1998).
 - ¹⁷ M. H. Hettler, J. Kroha and S. Hershfield, *Phys. Rev. Lett.* **73**, 1967 (1994); *Phys. Rev. B* **58** 5649 (1998).
 - ¹⁸ J. Kroha, *Adv. Solid State Phys.* **40**, 267 (2000). Note, however, that it is difficult to discriminate in this case two-

- channel Kondo scattering off TLS from ordinary single-channel scattering from magnetic impurities, as both mechanisms produce essentially the same scaling behavior of the energy distribution function [see, e.g., J. Kroha, report no. cond-mat/0102185].
- ¹⁹ H. Pothier, S. Gueron, N. O. Birge, D. Esteve, M. H. Devoret, Phys. Rev. Lett. **79**, 3490 (1997); F. Pierre, H. Pothier, D. Esteve, M. H. Devoret, J. Low Temp. Phys. **118**, 437 (2000).
- ²⁰ D. Berman, N. B. Zhitenev, R. C. Ashoori, and M. Shayegan, Phys. Rev. Lett. **82**, 161 (1999).
- ²¹ K. A. Matveev, Zh. Eksp. Teor. Fiz. **99**, 1598 (1991) [Sov. Phys. JETP **72**, 892 (1991)].
- ²² K. A. Matveev, Phys. Rev. B **51**, 1743 (1995).
- ²³ H.-B. Pang and D. L. Cox, Phys. Rev. B **44**, 9454 (1991).
- ²⁴ I. Affleck, A. W. W. Ludwig, H.-B. Pang, and D. L. Cox, Phys. Rev. B **45**, 7918 (1992).
- ²⁵ J. Ye, Phys. Rev. Lett. **77**, 3224 (1996).
- ²⁶ Note that, while the intermediate-coupling fixed point of the multi-channel Kondo model with more than two conduction-electron channels is also stable against exchange anisotropy, the Wilson ratio is no longer universal as in the one- and two-channel cases (see Ref. 25).
- ²⁷ For the anisotropic single-channel Kondo model, the Bethe ansatz equations have been recently solved in the range $J_z > J_\perp$. See T. A. Costi and G. Zaránd, Phys. Rev. B **59**, 12398 (1999).
- ²⁸ S. Chakravarty and J. Rudnick, Phys. Rev. Lett. **75**, 501 (1995).
- ²⁹ T. A. Costi and C. Kieffer, Phys. Rev. Lett. **76**, 1683 (1996); T. A. Costi, Phys. Rev. Lett. **80**, 1038 (1998).
- ³⁰ F. Lesage, H. Saleur, and S. Skorik, Phys. Rev. Lett. **76**, 3388 (1996);
- ³¹ S. P. Strong, Phys. Rev. E **55**, 6636 (1997).
- ³² E. A. Goremychkin, R. Osborn, B. D. Rainford, and A. P. Murani, Phys. Rev. Lett. **84**, 2211 (2000).
- ³³ R. Pietri, K. Ingersent, and B. Andracka, Phys. Rev. Lett. **86**, 1090 (2001).
- ³⁴ N. E. Bickers, Rev. Mod. Phys. **59**, 845 (1987).
- ³⁵ D. L. Cox and A. E. Ruckenstein, Phys. Rev. Lett. **71**, 1613 (1993).
- ³⁶ N. S. Wingreen and Y. Meir, Phys. Rev. B, 11040 (1994).
- ³⁷ B. Coqblin and J. R. Schrieffer, Phys. Rev. **185**, 847 (1969).
- ³⁸ S. Maekawa, S. Takahashi, S. Kashiba, and M. Tachiki, J. Phys. Soc. Jap. **54**, 1955 (1985).
- ³⁹ P. D. Sacramento and P. Schlottmann, Phys. Rev. B **43**, 1329 (1991).
- ⁴⁰ G. Zaránd, G. Zimányi, and F. Wilhelm, Phys. Rev. B **62**, 8137 (2000).
- ⁴¹ Note that, in the experiment of Ref. 20, e^2/C_B is equal to 0.46meV while $T = 260\text{mK}$, hence $e^2/C_B \approx 20k_B T$.
- ⁴² In the general case where the density of states in the quantum box and in the lead are asymmetric functions of energy with different functional forms, the position of the degeneracy point will typically shift from $\phi = e(N + \frac{1}{2})/C_B$. This shift can be absorbed, though, into a redefinition of the “magnetic field” eU .
- ⁴³ More precisely, $\chi(H, T)$ is the χ_{zz} component of the isospin susceptibility tensor.
- ⁴⁴ J. R. Schrieffer, P. A. Wolff, Phys. Rev. **149**, 491 (1966).
- ⁴⁵ A. A. Abrikosov, Physics **2**, 5 (1965).
- ⁴⁶ S. E. Barnes, J. Phys. **F6**, 1375 (1976); P. Coleman, Phys. Rev. B **29**, 3035 (1984).
- ⁴⁷ For a spin- $\frac{1}{2}$ impurity, the pseudo-fermion Green function is diagonal in the spin index, for arbitrary J_x, J_y , and J_z . This is no longer the case if $J_x \neq J_y$ and the impurity spin is larger than one-half.
- ⁴⁸ For convenience, we have omitted here a constant term, $\frac{M}{2} \sum_k J_0$, from the pseudo-fermion self-energy. The sole effect of such term is to shift the reference energy for the pseudo-fermion Green functions. It does not enter any physical observable.
- ⁴⁹ E. Müller-Hartmann, Z. Phys. B **57**, 281 (1984).
- ⁵⁰ P. D. Sacramento and P. Schlottmann, Phys. Lett. A **142**, 245 (1989).
- ⁵¹ Actually, different threshold exponents apply to $J_z = -|J_\perp|$ and $J_z < -|J_\perp|$, both of which differ from the characteristic exponents for the $J_z > -|J_\perp|$ “antiferromagnetic” case.
- ⁵² We note that an identical exponential dependence of the Kondo temperature as in the KNCA was obtained within Yosida’s variational wave function [K. Yosida, Phys. Rev. **147**, 223 (1966)], which likewise predicted an erroneous ferromagnetic Kondo effect. These flaws of the Yosida wave function were corrected in turn by going to more complicated variational wave functions, that included particle-hole excitations. For a detailed discussion, see K. Yosida, *Theory of Magnetism* (Springer-Verlag, Heidelberg, 1996), Chapter 17.
- ⁵³ H. Grabert, Phys. Rev. B **50**, 17364 (1994).
- ⁵⁴ D. S. Golubev and A. D. Zaikin, Phys. Rev. B **50**, 8736 (1994).
- ⁵⁵ H. Schoeller and G. Schön, Phys. Rev. B **50**, 18436 (1994).
- ⁵⁶ C. P. Herrero, G. Schön, and A. D. Zaikin, Phys. Rev. B **59**, 5728 (1999).
- ⁵⁷ The shoulders of the charge steps are smeared over a larger energy scale, governed by $\pi\rho t^2$.
- ⁵⁸ More specifically, for $H \neq 0$ the physics is that of a Fermi gas interacting with a spin-polarized scattering center. For a detailed discussion, see Ref. 13, Secs. 3.1.2, 4.2e, 5.1.4, 6.1.2, and 7.2.2.
- ⁵⁹ V. J. Emery and S. Kivelson, Phys. Rev. B **46**, 10812 (1992).
- ⁶⁰ G. Toulouse, Phys. Rev. B **2**, 270 (1970).
- ⁶¹ As pointed out by Sengupta and Georges [A. M. Sengupta and A. Georges, Phys. Rev. B **49**, 10020 (1995)], the leading irrelevant operator responsible for the $-T \ln(T)$ behavior of the specific heat is absent along the Emery-Kivelson line. Hence one has to deviate from this line to recover the $-T \ln(T)$ behavior of the specific heat. This does not apply to the susceptibility in response to a *local* applied magnetic field, which diverges logarithmically at the Emery-Kivelson line for vanishing T and H .⁵⁹
- ⁶² See, e.g., *Handbook of Mathematical Functions*, eds. M. Abramowitz and I. A. Stegun (Dover, New York, 1972), Chapter 6.
- ⁶³ J. Kroha, P. Wölfle, and T. A. Costi, Phys. Rev. Lett. **79**, 261 (1997); J. Kroha and P. Wölfle, Acta Polonica **B 29**, 3781 (1998).
- ⁶⁴ A. Furusaki and K. A. Matveev, Phys. Rev. Lett. **75**, 709

- (1995); Phys. Rev. B **52**, 16676 (1995).
- ⁶⁵ D. V. Averin and Yu. V. Nazarov, Phys. Rev. Lett. **65**, 2446 (1990).
- ⁶⁶ S. H. Pan, E. W. Hudson, K. M. Lang, H. Eisaki, S. Uchida, and J. C. Davis, Nature **403**, 746 (2000).
- ⁶⁷ A. Polkovnikov, S. Sachdev, and M. Vojta, Phys. Rev. Lett. **86**, 296 (2001).
- ⁶⁸ J.-X. Zhu and C. S. Ting, Phys. Rev. B **63**, 020506 (2001).
- ⁶⁹ For numerical convenience, we fixed ϵ_0 at each iteration by requiring that the integrated spectral weights of $a_{\uparrow}(\epsilon)$ and $a_{\downarrow}(\epsilon)$ add up to one.
- ⁷⁰ Similar to the NCA formulation for the Anderson model (see, e.g., Ref. 34), the magnetic vertex correction in the Coqblin-Schrieffer limit involves summation over an unpaired spin index that comes from the bare vertex. As a result, the magnetic vertex correction identically vanishes.
- ⁷¹ P. W. Anderson, J. Phys. C **3**, 2436 (1970).
- ⁷² The weak-coupling fixed point corresponds to a free spin. Therefore, the flow to weak coupling is signaled within the KNCA by the appearance of a zero-temperature delta peak in the pseudo-fermion Green function at the threshold energy, and the absence of a divergence in $\Delta(\epsilon + i\delta)$.
- ⁷³ Indeed, $\rho_0 A_{\mu}/[1 - A_{\mu}\Pi(D + i\delta)]$ with $\Pi(D + i\delta)$ evaluated to leading logarithmic order is the solution of Eq. (B9).